Joining of Shape-Memory NiTi Torque Tubes to Structural Materials

A Thesis

Presented in Partial Fulfillment of the Requirements for the Degree Master of Science in the Graduate School of The Ohio State University

By

Gordon R. Fox, B.S.

Graduate Program in Mechanical Engineering

The Ohio State University

2012

Master's Examination Committee:

Dr. Marcelo Dapino, Advisor

Dr. Amos Gilat

Abstract

Shape memory alloys (SMAs) have the potential to power small, lightweight, solid-state actuators through a thermally-induced phase transformation. Components of these materials can be "trained" via thermomechanical cycling to exhibit a shape memory effect, whereby the SMA acquires one geometric configuration in its high-temperature, austenite phase and another in its low-temperature, martensite phase. This transformation can be used to power an actuator. Nickel-Titanium (NiTi) is a shape memory alloy which is of interest because it can generate high stresses and relatively large strains through these thermomechanical processes. However, use of this alloy is hindered by the difficulty of integrating components made of it into structures and mechanisms made of other materials. Machining traditional joining features such as bolt holes and splines into NiTi pieces is difficult and expensive.

The objective of this research is to investigate processes for joining NiTi to structural materials such as aluminum and steel alloys. The processes presented here are ultrasonic soldering, adhesive bonding, laser welding, and tungsten inert gas (TIG) welding. Tubes of NiTi were joined to 304 stainless steel tubes and to aluminum 2024 blocks and tested in shear using a custom-made torsional testing machine.

There are two main sections to this thesis. The first section describes the development of a high-temperature torsional testing machine for characterization of the joints. This apparatus is used to determine the ultimate strength of the joints

and assess their resistance to creep and their performance during thermomechanical cycling.

The second section of this thesis describes the design and testing of the joints. Strength data, mechanical behavior plots, optical micrographs and hardness maps are presented. Lastly, the four joining methods are compared both qualitatively and quantitatively, and design guidelines are provided which can help establish the suitability of each process for different applications.

Acknowledgments

I would like to thank the contributors that made the research in this thesis possible. I am thankful to Dr. Marcelo Dapino, my adviser during my undergraduate and graduate studies at The Ohio State University. He provided guidance and encouragement throughout, recognizing and encouraging the good ideas that I had and questioning and improving the not-so-good ones. I would also like to thank Dr. Amos Gilat for reviewing this document and serving on both my undergraduate honors thesis and masters examination committees.

I would not have been able to do much of this work without the training and assistance of Ryan Hahnlen. He taught me much of what I now know about shape memory alloys, welding and joining processes, and testing equipment. The instruction and hands-on training that he provided are greatly appreciated!

This project would not be possible without the funding and technical guidance from Tad Calkins, Jim Mabe, and Tyler Zimmerman of the Boeing Company, Tim Frech and Steve Manring of the Edison Welding Institute (EWI), and the member organizations of the Smart Vehicle Concepts Center, a National Science Foundation Industry/University Cooperative Research Center (I/UCRC). The expertise in adhesives at Boeing and welding at EWI was extremely helpful, so that this project could focus on state-of-the-art joining processes. Without that, this research would have started out several steps behind where it did.

Vita

August, 1988 ..... Born - Wichita, KS

June 2006 ..... Diploma, Westerville South High School

June 2010 ..... B.S. Mechanical Engineering, The Ohio State University

Fields of Study

Major Field: Mechanical Engineering

Studies in Smart Materials and Structures: Dr. Marcelo Dapino

Major Field: Mechanical Engineering

Table of Contents

List of Tables

List of Figures

Chapter 1: INTRODUCTION

1.1 Thesis Organization

This thesis details research done on developing and testing methods for joining shape memory NiTi tubes to common structural materials, which will aid the integration of NiTi components into actuators and smart structures. The document is divided into two main parts: the first part (Chapter 2) describes the development of the high-temperature torsional testing machine that was used to test the joints, and the second part (Chapters 3 and 4) describes the design, construction, and testing of these bonds.

Chapter 3 describes the four different joining processes investigated and details their results, while Chapter 4 compares the processes, highlighting their relative strengths, weaknesses, and best applications. Equations and guidelines for designing NiTi joints with each of the four methods are given, as well as a summary chart in Table 4.1. Sections 3.3.6 and 4.6 describe work that will be performed in the future to build upon this research.

The work described in this thesis builds on prior research conducted in the Dapino group, as detailed by Hahnlen [8] and Hahnlen et al. [7, 9, 10]. Work described in this thesis that was primarily performed by Hahnlen includes:

- The development of the specimen and joint geometry for the ultrasonically soldered (USS), laser welded, and tungsten inert gas (TIG) welded joints, detailed in Sections 3.1.1, 3.2.1 and 3.3.1, respectively.

- Sectioning and optical microscopy of the specimens in Sections 3.2.3 and 3.3.3, for the laser and TIG welded joints, respectively.

- Hardness mapping of the sectioned specimens to identify heat affected zones, which is shown in Sections 3.2.3 and 3.3.4, for the laser and TIG welded joints, respectively.

The design and construction of the adhesive specimens, detailed in Section 3.4.1 and 3.4.3, was performed primarily at the Boeing Company.

1.2 Motivation for Research

Shape memory alloys (SMAs) can recover from large, seemingly plastic deformation upon heating. Through thermomechanical treatment they can be "trained" to have a low and high-temperature geometric configuration, which is called the two way shape memory effect. SMAs will transform to their high temperature configuration as they are heated through their austenite transition temperatures, and transform to their low temperature configuration when cooled across their martensite transition temperatures. These characteristic temperatures can be controlled by slightly varying the composition of the alloy.

The shape memory effect has potential to power actuators because the phase transformation can produce large stresses and strains. A commonly used shape memory alloy is nickel-titanium (NiTi) because of its high transformation stresses and strains,

as well as its low cost compared to other SMAs. For example, some of the NiTi tubes used in this research had a two way shape memory effect trained into them which enabled them to torsionally actuate over a 5% shear strain with a constant 20 ksi (140 MPa) shear stress. This is detailed in Section 3.3.5.

NiTi-based actuators have the potential to be smaller, lighter and simpler than comparable hydraulic or electric actuation systems in certain applications. These actuators are well-suited for high force, low displacement actuations that can be relatively slow. The bandwidth of these actuators is limited by the need to heat and cool the SMA to produce an actuation cycle. Boeing has used SMA actuators on their variable geometry chevron (VGC) to bend a chevron on the trailing edge of a jet engine into the exhaust stream to quiet the engine. Figure 1.1 shows a photograph of a VGC and the NiTi bar actuators used to bend it [13]. The constraints of integrating an actuator into a thin engine fairing made NiTi-based actuators ideal because of their small size. It was also found that the NiTi bars would actuate passively, so the actuator did not require an external power source. The temperature of the lower atmosphere is warm enough to heat the NiTi components into their austenite phase, and the temperature of an airliner's cruising altitude is cold enough to cool them into their martensite phase. Thus, engine noise is reduced on takeoff and landing by the chevrons actuating, and drag is reduced in cruise by the chevrons retracting [13]. All of this is accomplished with minimal weight, size and complexity added to the engine fairings. Although the VGCs are currently not used commercially, data gathered from their flight testing was used to design the fixed geometry chevrons on the engine fairings of production Boeing 787s.

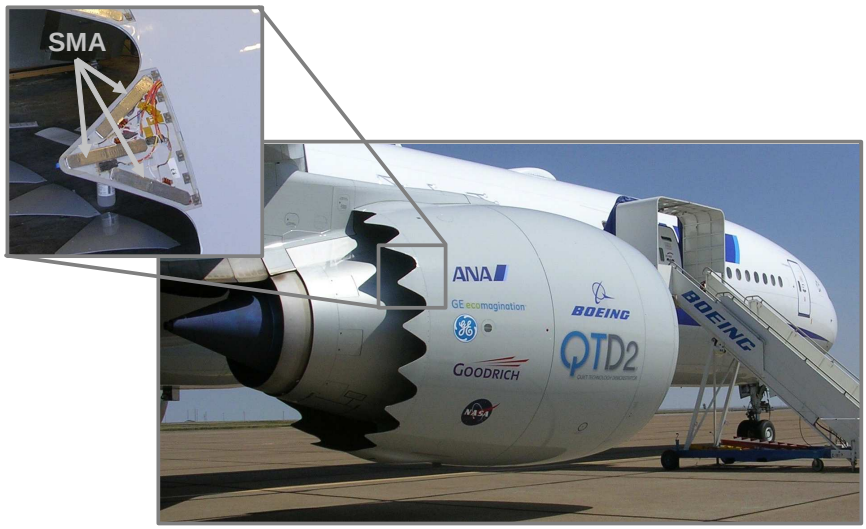

Figure 1.1: Boeing's variable geometry chevron.

Another application of NiTi-based actuators is for torque tubes to be placed inside helicopter rotor blades to change their twist profile "on-the-fly" to optimize it for different flight conditions. With this, a helicopter's hover payload and range can be increased dramatically. Currently, helicopter blades are designed as a compromise between the ideal configuration for hovering and for cruising. If that configuration could be changed mid-flight, then the blades could be optimal in both modes. NiTi power sources are appealing because of their small size and ruggedness, which are required for an actuator in the small, harsh environments inside a spinning rotor blade [15]. Such actuators have been made and tested, but difficulties were encountered in welding the NiTi torque tubes to titanium 6Al/4V attachments [14]. A photograph of a successful quarter-scale prototype of rotor blades using NiTi-based actuators is shown in Figure 1.2 [2].

Figure 1.2: Boeing's active rotorblade using NiTi torque tubes.

Currently, more applications for NiTi-based actuators are hindered by the difficulty of integrating NiTi components into structures and systems. If NiTi parts can be reliably and inexpensively integrated into larger actuation mechanisms, then some of the roadblocks preventing more widespread use of NiTi actuators would be eliminated. The focus of this research is therefore to enhance the integration of NiTi into structures through the investigation of methods to join NiTi to structural materials.

1.3 Previous Joining Issues

1.3.1 Machining Difficulties

Metal components are commonly joined into structures and mechanisms with mechanical methods such as threaded bolt holes or splines. Although mechanical methods are currently used to integrate NiTi parts into components and systems,

they are generally very difficult and expensive to make because of NiTi's extremely poor machinability. The high ductility and non-linear stress/strain behavior of NiTi cause chatter, high tool wear, and poor surface finish with many machining processes. Additionally, with processes that make a continuous cut such as turning on a lathe, unusually long chips can form and clog the machine. In a study of NiTi machining parameters on a CNC lathe, NiTi workpieces could be cut well only under very narrow cutting conditions. The carbide tools suffered heavy wear, and a 100 meter long cut was made without a single chip break [21]. A general rule-of-thumb for drilling holes in NiTi workpieces is that one new drill bit is needed for every hole that must be drilled.

Because of these issues, machining NiTi is usually done by grinding or electro discharge machining (EDM), which are more time-consuming and expensive processes than drilling, turning and milling. Boeing has made strong attachments by grinding splines onto the ends of NiTi tubes, an example of which is shown in Figure 1.3, however this costs several hundred dollars to do to each tube. If NiTi pieces could be joined to machinable materials such as steel or aluminum, such splines could be inexpensively rolled or cut into these pieces.

Several traditional machining processes were used on NiTi specimens for this research, usually for fixturing one end of a tube while a joint on the other end was tested. There were some features, however, that could not be machined well. The methods and features that were found to work the best are described in Section 4.5.

Figure 1.3: Splines ground onto a NiTi rod.

1.3.2 Heating Issues

The excessive heat produced by some joining processes can degrade or destroy the useful properties of a NiTi workpiece. The training and cold work originally in the NiTi workpiece may be partially recoverable through post-joining heat treatments and cold work, but these adds complexity and time to the joining process, and the properties will not be as good as if they were left undisturbed [20]. The two way shape memory effect can only be trained into NiTi pieces through extensive thermo-mechanical cycling, which is undone if the NiTi is annealed. NiTi loses its previous training and cold work if it is heated above 500°C (930°F) but it must be heated above 1300°C (2400°F) to melt in fusion welding processes [4]. Any heating of a NiTi workpiece must be localized to the area being joined, otherwise the training of the entire piece will be destroyed.

1.3.3 Hot Cracking

The melting and solidification of NiTi alloys in fusion welding can create problems. NiTi alloys, particularly if they are titanium rich, suffer from solidification fracturing, or "hot cracking." As the molten weld pool cools, NiTi solidifies first and begins to form grains, while Ni_2Ti remains liquid. The liquid Ni_2Ti moves between the NiTi grain boundaries and solidifies last, into a brittle compound. The thermal stresses of cooling create cracks in the Ni_2Ti phase which can propagate through the entire weld and create either a very weak joint or can cause joint failure even before the weld is done cooling [3, 20].

1.3.4 Cold Cracking

When fusion welding NiTi to ferrous alloys, the joints can suffer from a phenomenon called "cold cracking" in addition to hot cracking. This is where brittle intermetallics form in the weld pool, such as TiFe and $TiFe_2$, which have low strength at room temperature [19, 22]. The thermal stresses of cooling can create cracks at these points similarly to Ni_2Ti in hot cracking and result in the same poor weld strength.

Hall [11], found that both hot and cold cracking can be reduced through adding a nickel-rich filler metal to the weld pool. NiTi and ferrous alloys have been successfully welded together with this process. The Ni filler metal between the NiTi and ferrous workpieces keeps the Ti and Fe apart in the weld pool to prevent the formation of brittle intermetallics, and dilutes the Ti in the solidification zone to prevent hot cracking. This research has investigated two welding processes using this method: laser and tungsten inert gas (TIG) welding.

1.3.5 Oxide Layer in Soldering

The heating and cracking difficulties can be avoided with low temperature joining processes such as soldering. Soldering is a joining process where a low melting temperature joining alloy is melted onto the surfaces of two base metals, then the surfaces are brought into contact and cooled. The molten solder between the surfaces solidifies as they cool and joins them together. Neither of the base metals are melted.

Soldering NiTi is inhibited by the tough oxide layer that forms on its surface. This oxide layer prevents the molten solder from contacting the metallic surface and properly wetting it. Solder does not stick as well to this oxide layer as to a clean metal surface and weak joints result. Aggressive fluxes have been successfully used to solder NiTi [12], but these create health hazards and make the joining process and necessary cleanup more dangerous, difficult, and expensive.

1.4 Goal of Research

The overall goal of this research is to develop strong, reliable, low-cost methods for integrating NiTi components into larger actuation systems made out of common structural materials. Aluminum and stainless steel alloys were chosen to join with NiTi tubes because of their widespread use in aircraft. The techniques presented here are applicable to other materials as well. The four methods investigated were ultrasonic soldering (USS), adhesive bonding, laser welding, and tungsten inert gas (TIG) welding. Adhesives and soldering are the methods which are easiest to transfer to other materials. The welding processes probably could also be transferred to other materials, but they would require more modifications such as using different interlayers.

The intent of this research is to make torsional actuators, thus the NiTi components that were tested were tubes. These same processes could be used on NiTi wire in tension actuators and on arbitrarily shaped NiTi pieces in bending actuators or morphing systems. Because of the focus on torsion, shear strengths are reported instead of tensile strengths. No compressive or tensile tests are reported in this thesis.

Chapter 2: DEVELOPMENT OF TORSIONAL TESTING MACHINE

This chapter describes the development of a high temperature torsional testing machine used for mechanical testing of joints between NiTi and structural materials. Information on the joints and details of the results obtained with this machine are presented in Chapters 3 and 4. More information on the development of this machine can be found in [6]. A photograph of the machine is shown in Figure 2.1.

2.1 Machine Requirements

The required capabilities of the testing machine were determined by the geometry of the specimens that were to be tested. The tests were conducted on rods and tubes with an outer diameter of 0.375" (9.53 mm). This dimension was dictated by availability of NiTi specimens (supplied by industry partner Boeing), feasibility of creating the joints (done in collaboration with Edison Welding Institute), and practicality of the experiments. From this diameter, the breaking torques of a solid stainless steel and aluminum rod were calculated. Regardless of the capabilities of the testing machine, no joint with these materials could be tested beyond that torque because the base metals would break first.

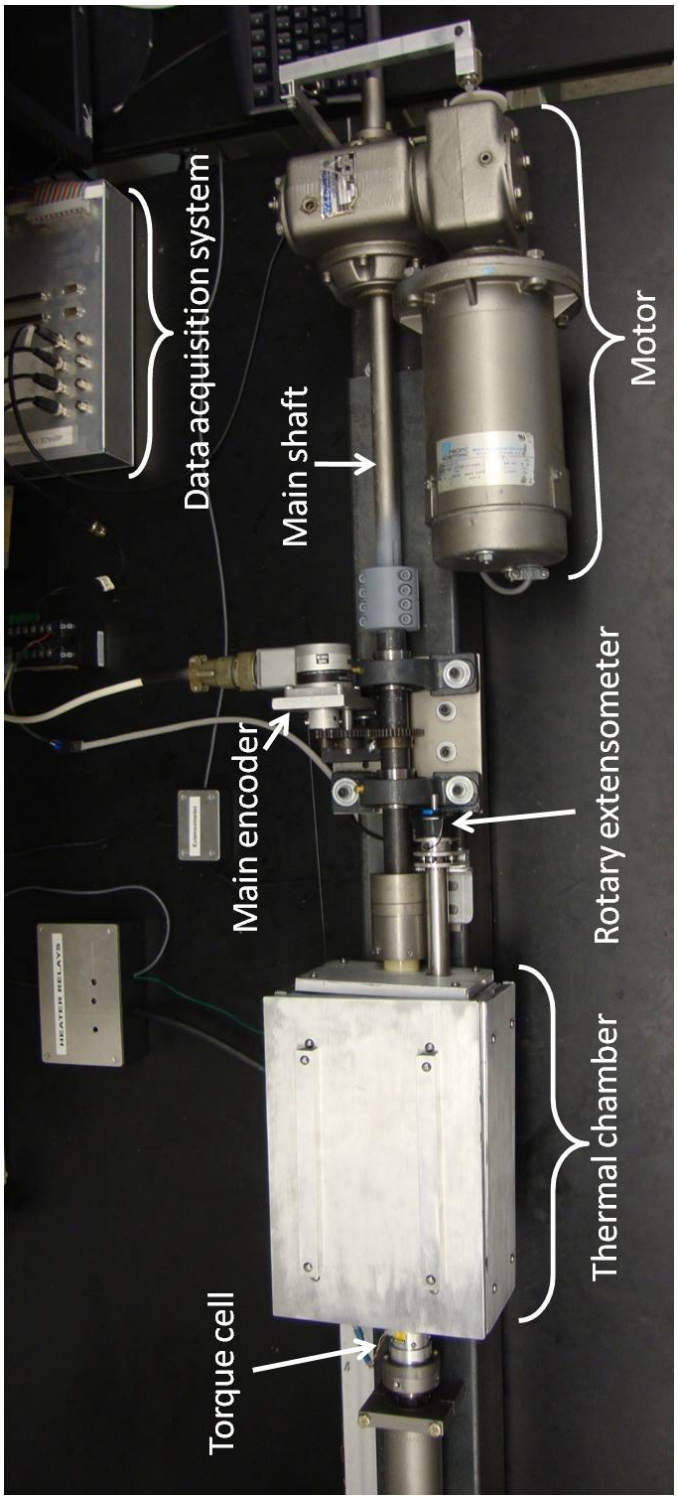

Figure 2.1: Overview of torsional testing machine.

The breaking torque of a homogeneous tubes in simple torsion is given by

$$\tau_{max} = \frac{T_{max} \times r_o}{J}, \tag{2.1}$$

where

$$J = \frac{\pi}{2}\left(r_o^4 - r_i^4\right). \tag{2.2}$$

Here, τ_{max} is the ultimate shear strength of the material, T_{max} is the breaking torque, r_o is the outer radius, and r_i is the inner radius of the specimen. For the geometry being considered, $r_o = 0.375$" (9.53 mm) and $r_i = 0$. The values of τ_{max} for annealed 304 stainless steel and aluminum 2024-T3 are 49 ksi (340 MPa) and 40 ksi (280 MPa), respectively [5]. These shear stresses give breaking torques of 510 in-lb (57 N-m) and 420 in-lb (47 N-m), respectively. The machine was thus designed to apply at least 510 in-lb (57 N-m) of torque.

The maximum temperature that the thermal chamber had to achieve was at least the highest transition temperature of the shape memory alloy being studied. The NiTi supplied by Boeing was equi-atomic (55 weight% Ni, 45 weight% Ti) which has transition temperatures no higher than 100°C [18]. The austenite finish temperature, A_f, of most of the tubes used was 80°C. Since the ultrasonic soldering process takes place at 250°C, it was necessary to conduct tests up to at least that temperature. Based on these considerations, the thermal chamber was designed to be able to reach 300°C (600°F).

The testing machine was also designed to be able to thermally cycle specimens for lifespan tests of joints. Cooling an SMA is usually the longest part of an actuation cycle, so shortening the cooling time greatly increases the number of thermal cycles that

can be run in a given time. There was no fixed goal for the cooling capabilities other than that they should be as fast as possible. The loose goal of 10 minutes per cycle over the transition temperature range of the NiTi tubes (20 to 100°C) was employed in the design of the cooling system.

2.2 Specimen Fixturing

Since NiTi is difficult to integrate into mechanical systems, fixturing NiTi tubes into the torsional testing machine is challenging. Three different methods have been used for fixturing: friction clamps, pin-hole grips, and joined grips.

2.2.1 Friction Clamps

Friction clamps are attractive because they require no machining to fixture a NiTi tube. These clamps are reusable grips that clamp onto the outside of a plain NiTi tube which apply force radially to the tubes to create enough friction to hold them in place while a torque is applied. NiTi has a low coefficient of friction with grip materials (such as steel and aluminum), so it is very difficult to grip NiTi tubes via friction.

The basic design of the clamp grips is two halves, each with a semi-circular hole on the side where they meet, held together by cap screws. The exact geometry and the number of screws varied from iteration to iteration. A photograph of the four-screw design is shown in Figure 2.2.

The cap screws on the clamp can only be tightened to 90 in-lb (10 N-m) without yielding the steel at critical points in the clamp, so this limits the clamping force. This four-screw design is still able to grip aluminum tubes tightly enough to torque them to failure, but cannot grip stainless steel or NiTi tubes as well because they do

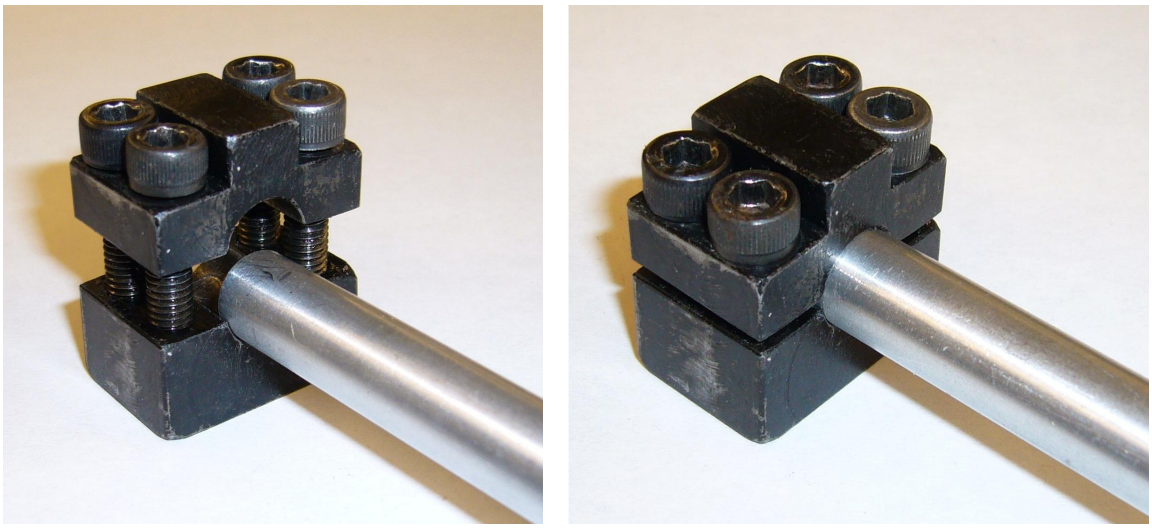

(a) Open grip (b) Closed grip

Figure 2.2: Four-screw friction grip specimen fixture.

not have as high of a coefficient of friction with steel as aluminum does. When this grip is used on stainless steel and NiTi tubes it can only transmit about 250 in-lb (28 N-m) of torque before slipping, which is not enough to break the tubes or fail most joints. To counteract this problem, an eight-screw design was built, which is shown in Figure 2.3.

The eight-screw design did not perform as expected; it started to slip when applying 450 in-lb (51 N-m) of torque. Also, it is 1.25" (32 mm) long, which is about 0.75" (19 mm) longer than the four-screw and pin grip designs. This means that any specimen which is designed to be gripped by the eight-screw clamp must have a 0.75" longer NiTi tube in it than with a pin grip. This makes the specimens more expensive. Friction grips were only used on tests where the failure torque was expected to

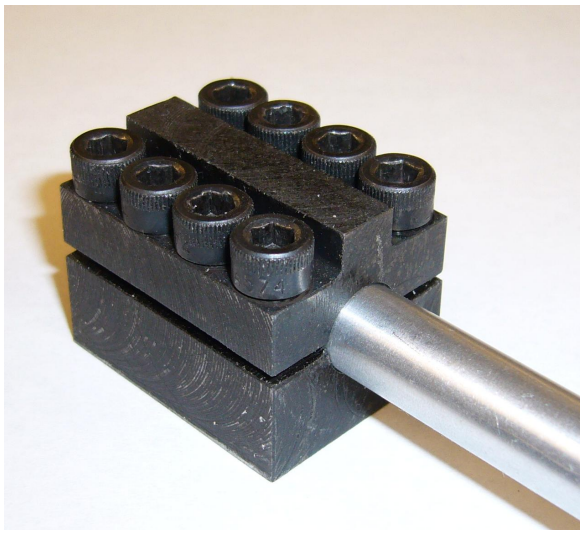

Figure 2.3: Eight-screw friction grip specimen fixture.

be less than 250 in-lb (28 N-m), which were the thin-walled laser weld tests and a few of the high-temperature adhesive tests.

2.2.2 Pin-Grips Holders

Although it is desirable to avoid machining mechanical gripping mechanisms into NiTi tubes, drilling a pin hole in NiTi tubes has proven to be the best way to fixture them. These pin grips use a 1/8" (3.2 mm) diameter pin hole drilled through both sides of the tube walls, then a steel pin is inserted through a hole in the grip block and tube. A pin grip is shown in Figure 2.4.

Although drilling the pin hole presents challenges, satisfactory processes and tools were developed to accomplish this task, which are detailed in Section 4.5. Another problem which was encountered, however, was cracks initiating in poorly-drilled pin holes. In one of the adhesive specimens, a crack initiated at a defect in the pin hole and propagated helically along the NiTi tube and through the NiTi surface that

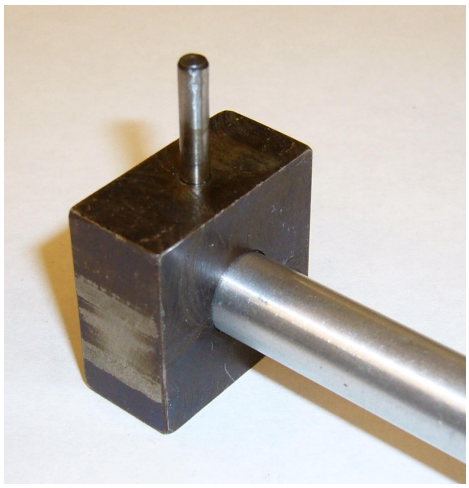

Figure 2.4: Pin grip specimen fixture.

was bonded to the aluminum grip. This caused premature failure of the joint and prevented obtaining accurate shear strength data from that specimen. A photograph of this failure is shown in Figure 2.5. With properly drilled holes, these pin grips were shown to apply over 500 in-lb (57 N-m) of torque to NiTi, 304 SS and Al 2024 tubes without failure.

The material in the tube contacting the pin is subjected to much more stress than the nominal stress in the tube due to torsion. This causes yielding of this material at a much lower torque than in the rest of the tube. (Several specimens have been made with a reduced diameter in a gauge region, but most of the specimens have had a uniform cross section along their length). The effect of this additional stress was investigated by analyzing a simplified model of the pin and tube wall interaction. As shown in Figure 2.6, the contact between the pin and tube wall was assumed to occur on a flat plane of width d, which is the diameter of the pin, and height wt, which is the wall thickness of the tube. The force, F, is assumed to be constant over this

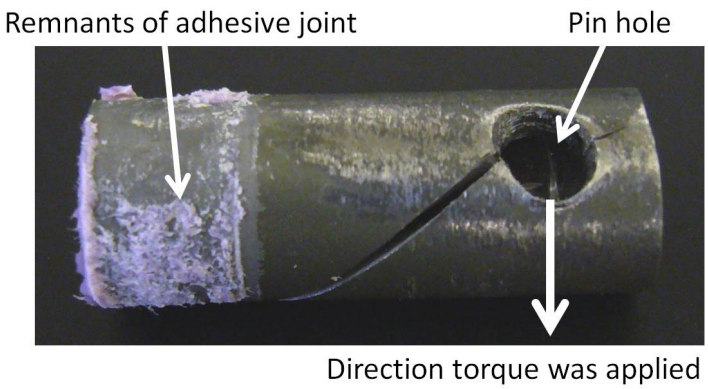

Figure 2.5: Failure in adhesive specimen due to poorly made pin hole.

area. This simplified model ignores the curved interface between the pin and tube wall and the variation in force over the radius of the tube, but still gives a reasonable approximation of the stress amplification at this point observed experimentally.

The stress at the tube/pin interface comes from two sources: the bearing force of the pin on the pin hole and the shear stress from the torque on the tube. These stresses are calculated and combined into an equivalent von Mises stress. The bearing force is related to the torque on the tube by

$$T = F \times d_F \tag{2.3}$$

where F is the bearing force and d_F is mean distance between the two areas where the force is applied. The mean distance is

$$d_F = D - wt. \tag{2.4}$$

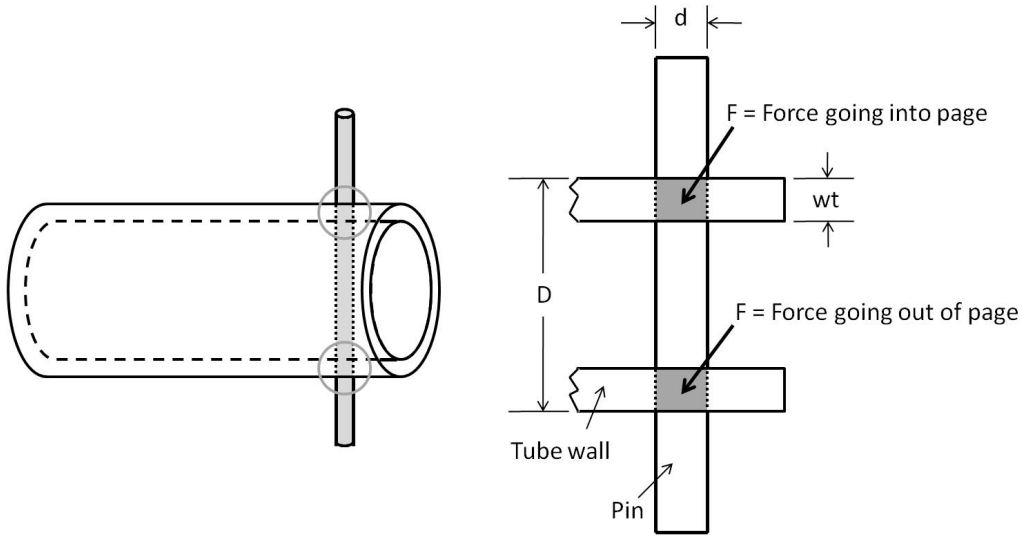

Figure 2.6: Analysis of simplified pin grip and tube wall interaction.

The stress due to the bearing force, σ_b, is

$$\sigma_b = \frac{F}{A} \tag{2.5}$$

where the area of the interface region is $A = d \times wt$. Another consideration is that the stress concentration factor for a 1/8" diameter pin hole in a 3/8" diameter shaft in torsion is approximately 1.4 [5]. Combining all this, one gets

$$\sigma_b = \frac{1.4 \times T}{(d \times wt)(D - wt)}. \tag{2.6}$$

The expression for the shear stress, (2.1) becomes

$$\tau_n = \frac{16 \times T \times OD}{\pi \times (OD^4 - ID^4)}. \tag{2.7}$$

Equations (2.6) and (2.7) can be combined into an equivalent von Mises stress. This stress, σ_i, is the stress at the tube/pin interface. The full von Mises equation is

$$\sigma_{eq} = \sqrt{\frac{(\sigma_{11} - \sigma_{22})^2 + (\sigma_{22} - \sigma_{33})^2 + (\sigma_{11} - \sigma_{33})^2 + 6(\sigma_{12}^2 + \sigma_{23}^2 + \sigma_{31}^2)}{2}}, \tag{2.8}$$

where σ_{eq} is the equivalent stress, σ_{11}, σ_{22}, and σ_{33} are the normal stresses and σ_{12}, σ_{23}, and σ_{31} are the shear stresses. Here, $\sigma_{11} = \sigma_b$ and $\sigma_{12} = \tau_n$. All of the other stresses are zero, and (2.8) then reduces to

$$\sigma_i = \sqrt{\sigma_b^2 + 3\tau_n^2} \tag{2.9}$$

where σ_b is calculated from (2.6), and τ_n is calculated from (2.7). This is now compared to the nominal stress from simple torsion to find the stress amplification created by the pins.

The shear stress from (2.7) can be related to an equivalent tensile or compression stress, σ_{eq}, by the von Mises equation. For simple shear, the full von Mises criterion (2.8) reduces to $\sigma_{eq} = \tau\sqrt{3}$. Therefore, the nominal shear stress calculated by the von Mises criterion is

$$\sigma_n = \frac{16\sqrt{3} \times T \times OD}{\pi \times (OD^4 - ID^4)}. \tag{2.10}$$

The stainless steel tubes used in this study had an inner diameter of 0.245", which corresponds to $wt = 0.065$" (1.65 mm), and most of the NiTi tubes in this study had an inner diameter of 0.225", corresponding to $wt = 0.075$" (1.90 mm). From this, the stresses at the pin/tube interface were calculated to be 2.9 and 2.8 times larger than the nominal stress in the stainless steel and NiTi tubes, respectively.

This effect can be seen in the experimental data, such as the plot of torque versus angle for plain 304 SS and NiTi tubes, shown in Figure 2.7. The torque versus angle curve of the 304 SS tube is linear at first, then decreases in slope at 80 in-lb (9.0 N-m). It is then linear again until around 195 in-lb (21.5 N-m). The first decrease in slope is from the material at the pin hole starting to yield. The rest of the tube starts to yield at the second decrease in slope. The ratio of these two torques is 2.4, close to the 2.9 predicted by the simplified model of the pin/tube interaction. This effect is the same in the NiTi data as well. All of the data taken with these pin grips shows the same effect, an initial yielding (or detwinning if the specimen is NiTi) in the material around the pins, then a general yielding in the entire tube at a torque approximately 2.5 times higher. Even with this stress concentration, failure never occurred at properly drilled pin holes. The joints always failed before the material at the pin holes failed. Therefore, these pin grips are suitable for obtaining strength data, but not for stiffness data, unless a gauge is mounted directly to the specimen, like the rotary extensometer discussed in Section 2.3.2.

2.2.3 Joined Grips

The last method used to fixture specimens into the torsional testing machine was to join a grip to the NiTi tube in addition to the grip being tested. This second fixturing grip must be joined with a significantly stronger joint than the first testing grip so that it does not fail before the first. This method was only used for the ultrasonic soldering tests. A specimen from those tests is shown in Figure 2.8. This method could also have been used for the adhesive tests since NiTi tubes were joined to aluminum blocks in both cases, but it was easier to use reusable pin grips on the

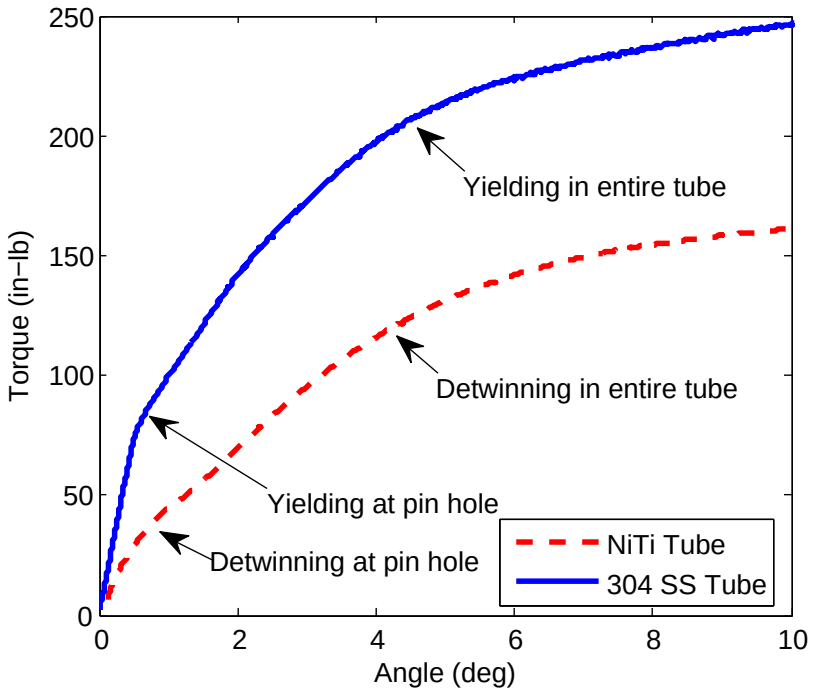

Figure 2.7: Test results of plain NiTi and 304 SS tubes using pin grips.

non-joined end of the NiTi tube rather than making twice the number of aluminum grip blocks and adhesive joints.

2.2.4 Square Grip Holders

The square clamp grips, pin grips, and blocks joined to the NiTi tube were held in square holes in the torsional testing machine. In the USS and laser welding tests these were square holes in couplers to the main shaft of the machine, which applied the torque, while in the TIG and adhesive joining tests the holders were blocks that had two V-grooves which clamped together to hold the square more tightly. These are shown in Figure 2.9.

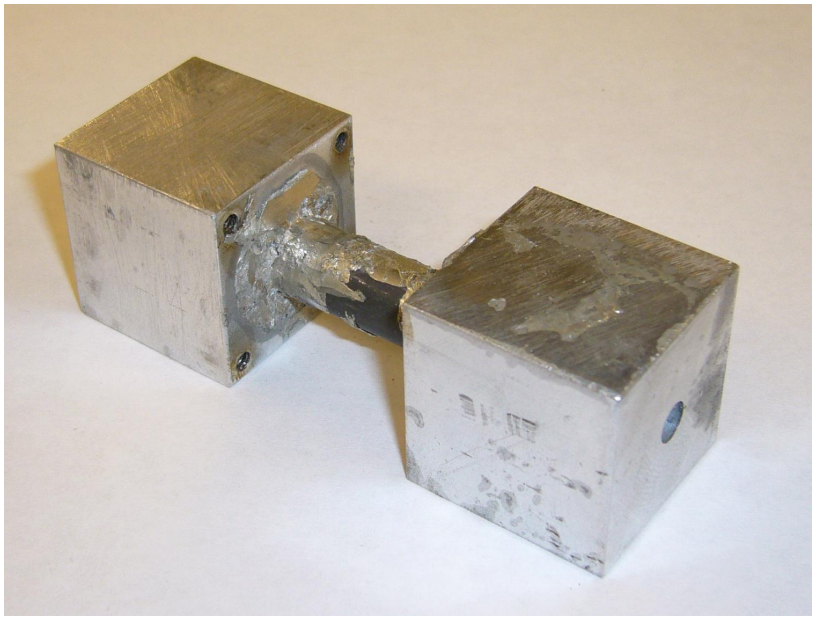

Figure 2.8: Joined grip specimen fixture.

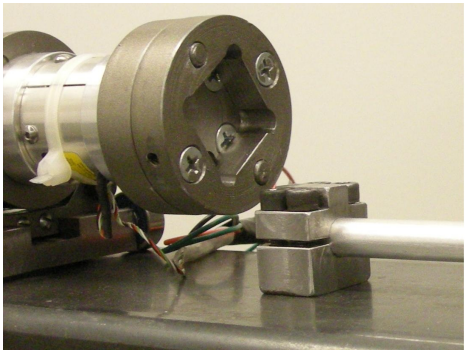

(a) Square hole holder.

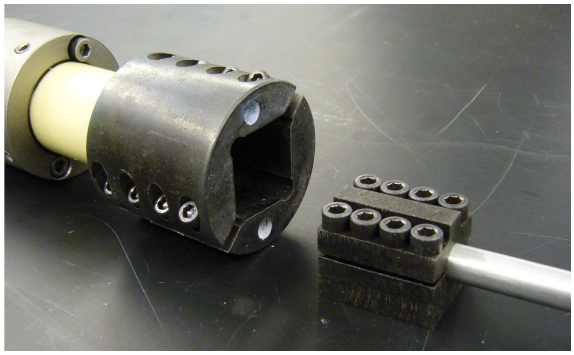

(b) Double v-groove holder.

Figure 2.9: Square block fixtures.

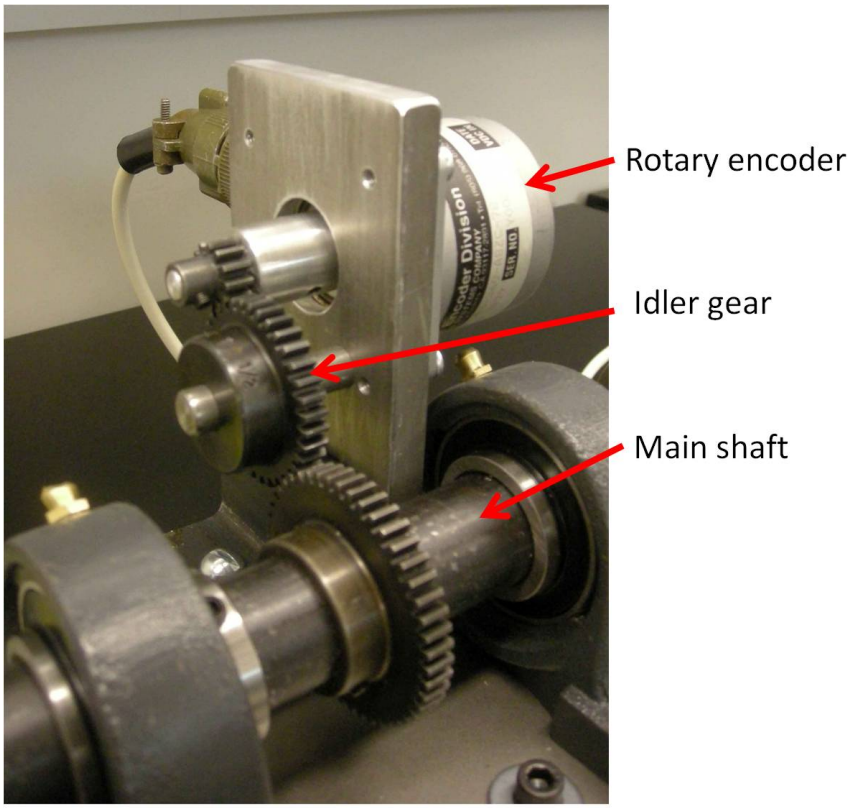

Figure 2.10: Main shaft rotary encoder.

2.3 Deflection Measurement

In order to obtain accurate stiffness data and control the torsional machine during tests, accurate deflection measurement is needed. There are two methods used to measure deflection: a rotary encoder connected to the main shaft of the machine, and a custom-built rotary extensometer which mounts directly to a gauge region on the specimen.

2.3.1 Main Shaft Rotary Encoder

To measure the deflection of the main shaft of the machine, a rotary encoder is connected to it via a series of gears, as shown in Figure 2.10. Backlash between the gears connecting the encoder to the machine can cause inaccurate readings, especially when the motor starts or changes direction. To fix this, a constant-force spring is attached to the encoder shaft to provide a constant torque, enough to eliminate the backlash in the gears. As the encoder shaft spins, the spring wraps around it, providing a similar effect as if a string was attached to a suspended weight. With this system the backlash is eliminated.

The main shaft rotary encoder can be used to infer specimen deflection during tests, but it includes deflection of the load train and grips. This is especially significant if using the pin grips, described in Section 2.2.2. If the behavior of the machine and pin grips was known, it could be subtracted from the measured deflection leaving only the specimen's deflection. However, the deflection around the pin holes in the specimens cannot be measured or predicted accurately. A uniform diameter stainless steel tube was tested with pin grips its behavior was not exactly repeatable test-to-test above the yield torque of the material around the pins. The material work-hardened as one would expect, the first cycle was less stiff than subsequent cycles, but it did not stiffen in an easily predictable way. If stainless steel was that difficult to predict, NiTi would be even more difficult with detwinning and recovery in addition to plastic deformation. Because accurate deflection data of specimens could not be inferred from the main shaft rotary encoder, a rotary extensometer was made to clamp directly to the specimens.

2.3.2 Rotary Extensometer

The extensometer, which mounts directly to the specimens, eliminates the grip effects, measuring only the deflection of a gauge region on the specimen. It can handle high strains (NiTi tubes can strain up to 8% without yielding), high temperatures (up to 300°C, 600°F), and repeated cycles for thermomechanical cycling tests. Off-the-shelf strain gauges and extensometers can meet two of the criteria, but not all three.

No potentiometer or rotary encoder could withstand the temperatures of the thermal chamber, so two shafts were used to transfer the motion of the specimen outside of the thermal chamber to where it is measured. Each shaft is connected by gears to the specimen at a different location, so the difference in rotation of the two shafts indicates the rotation between the two locations. Large gears are mounted at two locations on the specimen, and smaller gears which mesh with these are connected to the inner and outer shaft of the extensometer. One smaller gear is on a shaft connected to the input of a rotary encoder while the other gear is on a shaft connected to the housing of the encoder. With this setup, the encoder measures the difference in rotation of the two shafts. The two shafts are co-axial, so one is hollow and encircles the other. This design is illustrated in Figure 2.11, and a photograph of the extensometer is shown in Figure 2.12.

The large gears have screw holes for mounting to tapped holes either in grips like those soldered or adhered to the NiTi tubes, or to removable mounts which temporarily attach to the NiTi tubes. The gears have a 1" (25.4 mm) square hole machined in the center of them so they can slide over 1" square grips like the USS and adhesive grips. The temporarily attachable mounts are made so that they can be

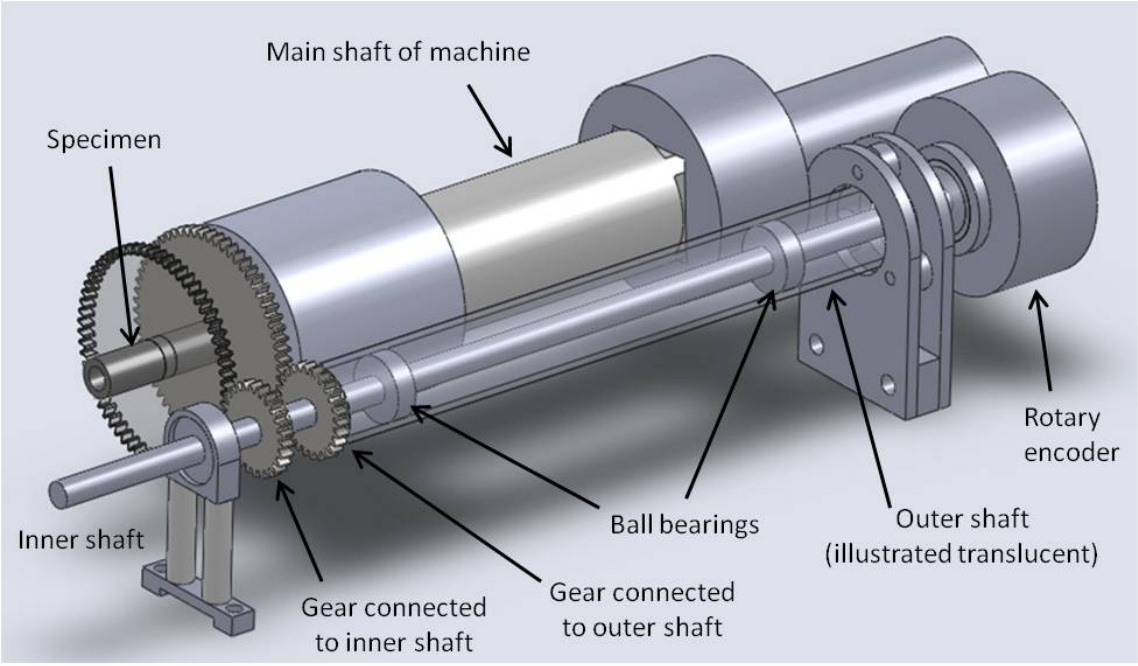

Figure 2.11: Diagram of rotary extensometer.

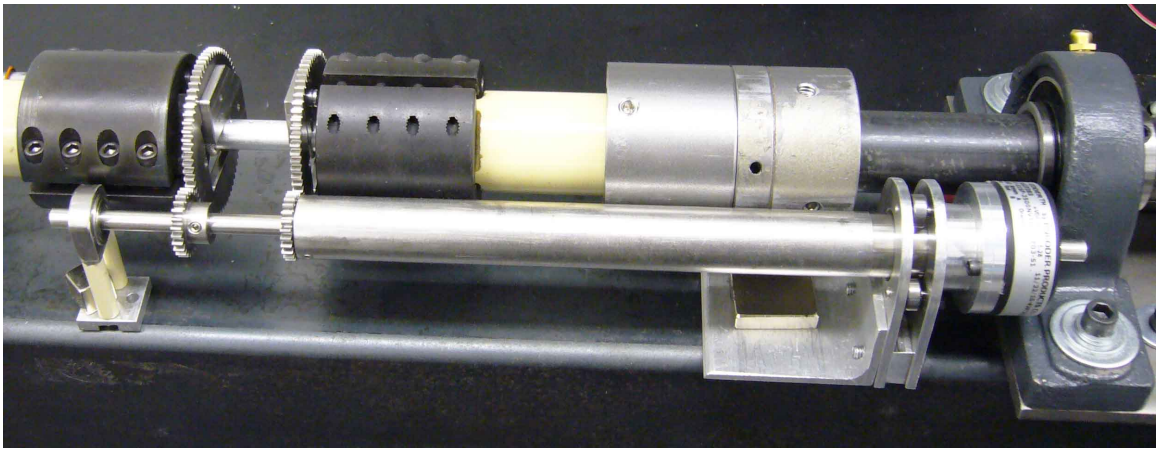

Figure 2.12: Photograph of rotary extensometer.

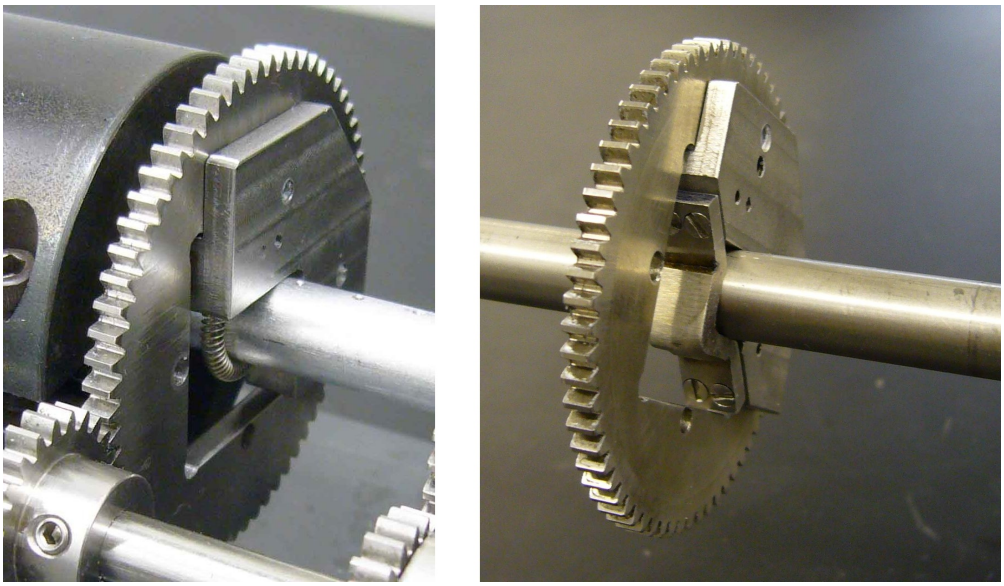

(a) Spring grip. (b) Clamp grip.

Figure 2.13: Rotary extensometer gear mounts.

precisely located on a tube, and grip firmly for the duration of a test. Springs have been used to hold these grips to a specimen, but are generally too weak, so clamps are mostly used instead. Both of these designs are shown in Figure 2.13.

The gear mounts have a V-groove that butts up against the outside of the specimen, and two cone-pointed set screws that jut out of the V-groove surfaces. These make the point of contact known, because otherwise the mount and the tube would have line contact along the axis of the tube, and it would not be known where along that line the mount was moving with the deforming tube. These set screws work best when tiny starter holes are drilled in the outside of the tube for them to seat in. These holes can be precisely spaced on a mill, which allows the gauge region of this extensometer to be precisely set.

2.4 Torque Measurement

Torque was measured during all tests with a Futek TFF350 reaction torque sensor. This torque cell can be seen in Figure 2.9(a) immediately to the left of the square hole holder. It uses strain gauges mounted to an aluminum tube. It is periodically calibrated with a moment arm. The moment arm is placed onto the main shaft of the torsional machine in place of the motor, and adjusted so that it is level before weight is applied. The torque cell is calibrated before each round of testing.

The torque cell was coupled to a Labview data acquisition system with a NI 9297 input module for the tests of USS, laser and TIG welded specimens. For the adhesive specimen tests it was coupled to a dSPACE 1104 control and data acquisition system with a Omega DMD-465WB strain gauge exciter and amplifier.

After measurement, the torque data is fed through a digital low-pass filter to remove high frequency noise, such as 60 Hz electrical noise. Because all tests are run with a ramp torque, the signal corresponding to the physically applied torque is not attenuated by this filter.

2.5 Torque Application

Torque is applied to specimens by a DC motor and gearbox. The output of the gear box is connected to the main shaft of the torsion machine. One side of the specimen is held stationary while the other is rotated by the main shaft. The USS, laser and TIG welding tests were run with open-loop control of the motor, while the adhesive and all ongoing tests use feedback control. Two different types of controllers are currently used for different types of tests and are described here.

2.5.1 DC Motor

The DC motor has a maximum voltage of 90 V and a no-load speed of 1800 rpm. It is immediately connected to a 500:1 gear reduction, the output of which is connected to the main shaft of the machine. With the gear box, the no-load speed of the main shaft of the machine is about 3 rpm, though tests are usually run at 0.5°/s, or 1/12 rpm. The motor and gearbox can be seen in Figure 2.1.

2.5.2 Torque-Based Controller

A torque-based controller is used during constant torque tests. These are free heating-recovery tests of NiTi tubes, and constant torque creep tests. A proportional and integral (PI) controller provides sufficient stability and quick enough transient response for these applications. A block diagram of the controller used is shown in Figure 2.14.

The dynamics of the motor are sufficiently fast that the motor transfer function, $G(s)$ can be approximated as a constant. This is because there is almost no inertia acting on the motor, especially with the 500:1 gear reduction between the motor and the rest of the machine. The sensitivity of the motor is about 0.21 (°/sec)/V with a dead zone between -2 and +2 V. This means that a 5 V input will produce a speed of about 0.63 °/sec. The PI controller is sufficiently robust to perform well even with the non-linearity of the dead zone.

The controller has additional logic in addition to simple PI control to avoid saturation if the command torque is changed by the operator suddenly, or the controller is switched on when the actual torque is far away from the input torque. If the error (reference minus measured torque) is greater than 1.5 in-lb, the system uses open-loop

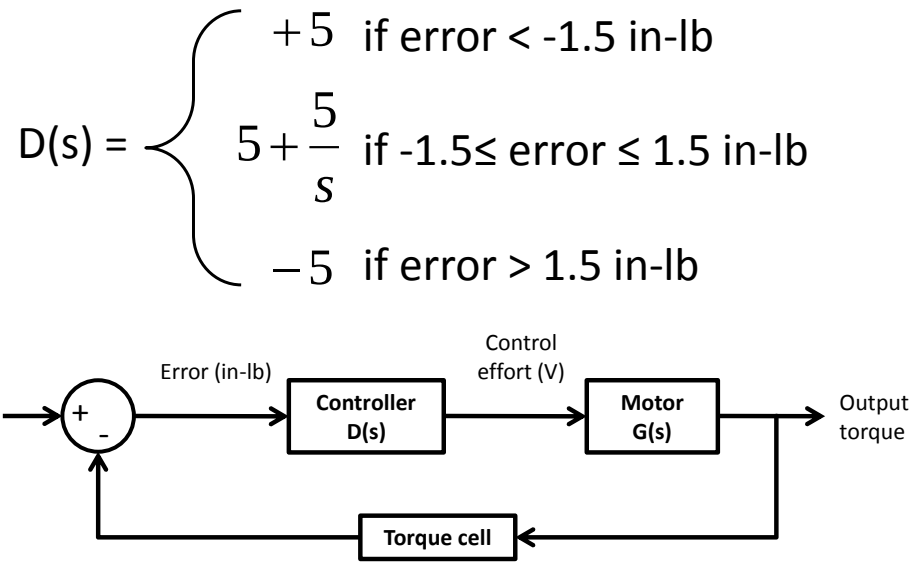

Figure 2.14: Block diagram of torque-based controller.

control to bring the torque to within 1.5 in-lb, after which PI control is activated. This produces a smooth approach to the reference torque from a point arbitrarily far away. There is also logic in the programming of the controller so as to not saturate the integrator in the PI controller while this controller is turned off or open-loop control is taking place.

2.5.3 Deflection-Based Controller

A controller that is able to apply a ramp deflection was designed for strength tests. Due to the non-linear stiffness of the NiTi in the specimens, a ramp reference torque could not be inputted to the torque-based controller and have the machine output a ramp deflection.

Using the output of the angular encoder as feedback to compare with a reference angle does not work well. The problem with this approach is that the angular encoder

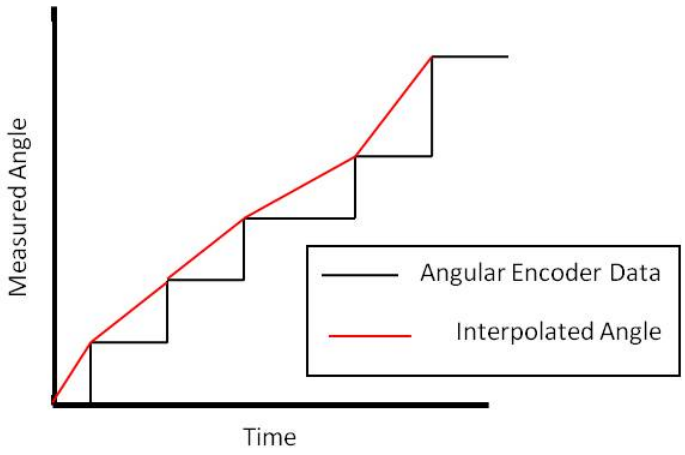

Figure 2.15: Illustration of stair-step output of angular encoder.

outputs a quantized signal instead of a continuous signal, which is illustrated in Figure 2.15. When using the encoder data to calculate stiffness from test data, this is accounted for by interpolating between the points of the "stair steps." This cannot be done in real time because it requires knowledge of when the next stair step will occur. When this type of feedback data is fed into a controller it produces a strongly unstable control effort. While turning the gain down somewhat mitigates this instability, doing so comes at the expense of poor tracking.

This problem is fixed by adding an analog tachometer to "fill in" the stair steps in real time. Although this tachometer is very noisy and not as accurate as the angular encoder, it effectively fills in the stairs to permit smooth operation of the motor with a control gain high enough to quickly follow a reference input. The tachometer is a small DC motor mounted to the main motor shaft, before the gear reduction, with its own gears to amplify the motion to produce a larger signal. A photograph of this is shown in Figure 2.16. Its output is very noisy, but since its output is integrated to

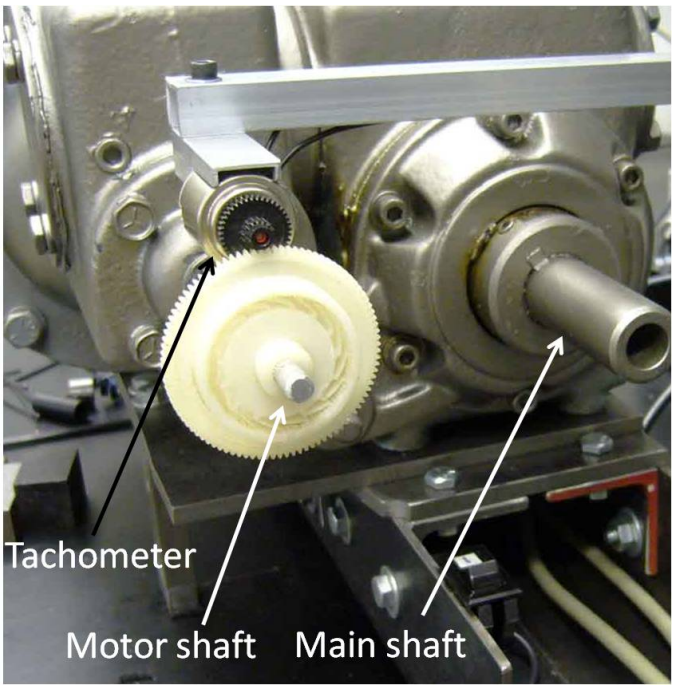

Figure 2.16: Photograph of tachometer.

give position, this integration removes most of the noise. Test data taken using this hybrid controller is shown in Figure 2.17.

The motor controller is programed and run in dSPACE. The program takes the last known point from the digital angular encoder and estimates the change with the analog tachometer until the encoder reaches its next bit of resolution. If the interpolation exceeds ±1 resolution bit of the angular encoder before that point is reached, it saturates there until that step is reached, then the estimation starts over again. In Figure 2.17 there is a point where the angular encoder measures the next stair before the estimation was expecting it. The angle immediately jumps to that point and starts estimating again. Later, the estimation reaches +1 resolution bit

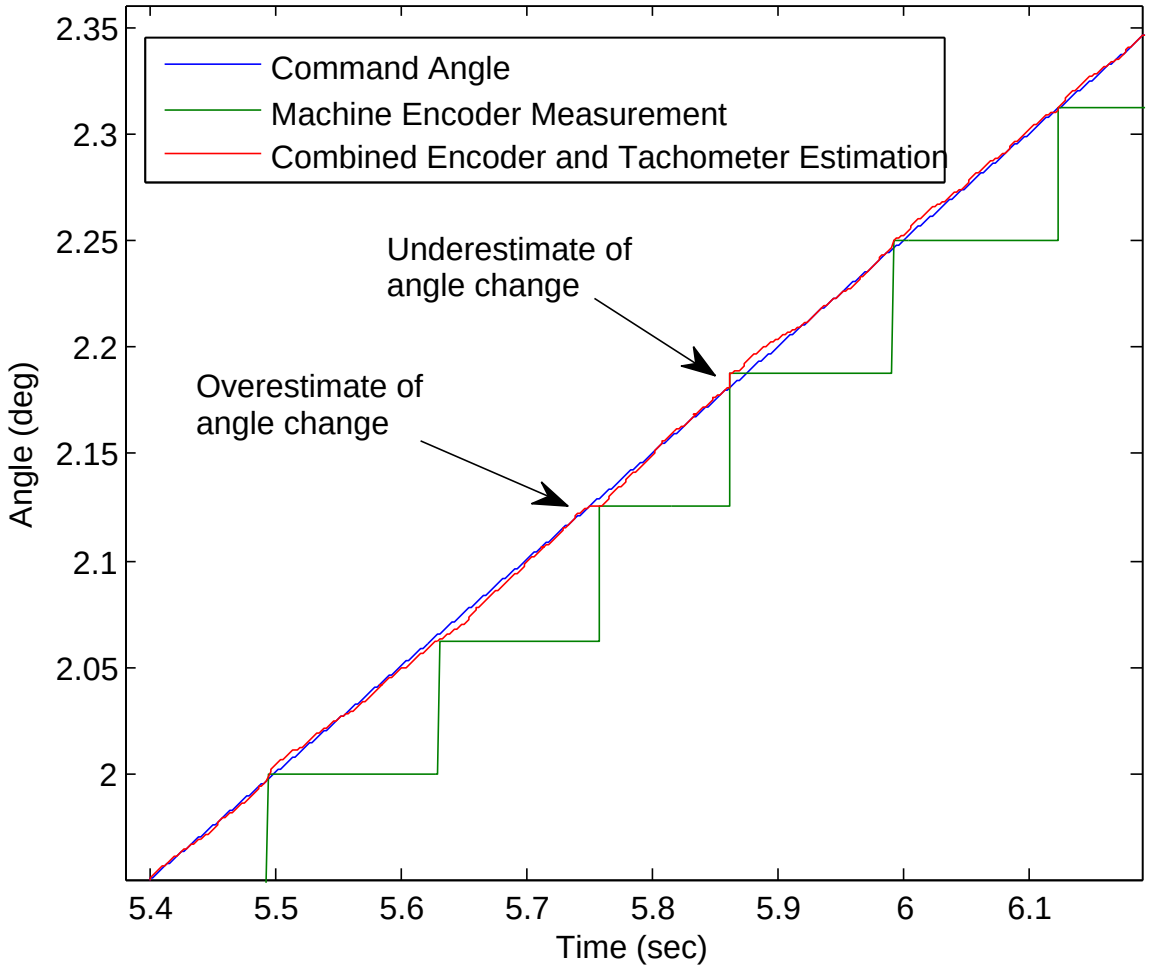

Figure 2.17: Test data of hybrid encoder / tachometer controller.

from the last stair before the angular encoder measures that stair, so it saturates there waiting for it.

The position controller is effective and was used for the adhesive tests. That being said, it often has a jerky start due to system backlash. Error would accumulate while the motor was running and the backlash was being taken out, but the encoder was not moving. This was not a problem with the encoder itself, but with play in the main shaft of the machine. This would cause a spike in control effort which would quickly die away and then the controller would then function well. To prevent this from affecting the data, tests were usually started at -10 in-lb, then the controller was turned on to $+0.5°$/sec. By the time the torque became positive, this spike would have died out and the test proceeded smoothly.

Also, while running hundreds of torque cycles on non-important trial specimens to observe the performance of the controller, in about one out of every hundred torque cycles the controller would change direction briefly then resume normal operation with a spike in control effort similar to the worst start-ups. It would do this during unloading, so it never affected the adhesive failure tests. This was probably caused by the estimator not properly handling some unexpected events in the decreasing torque phase, and having the control gain too high.

The position-based controller could probably have been modified (and made even more complicated than it had already become) to fix these problems, but a simpler solution was implemented instead. Real-time control is based entirely on the tachometer, while post-test data analysis is based on the more accurate angular encoder. This new controller is velocity-based instead of position-based like the previous one, so it

is not quite as capable, but works sufficiently well for applying a constant velocity, which is all that the tests require.

With the velocity-based controller the tachometer measures velocity, which is not integrated to give position as it was in the position-based controller, the tachometer's noise is a problem. To fix this, an analog low-pass filter conditions the signal before the data acquisition system.

2.6 Thermal Measurement

The temperature of the specimen was measured with thermocouples during elevated temperature tests. These were type K thermocouples and used an Analog Devices AD 8495 amplification and cold junction compensation chip to interface with the dSPACE data acquisition system. The output of the amplification chips was calibrated against an Omega model HH22 thermocouple reader before any tests were run using them.

2.7 Thermal Controller

A feedback thermal controller controls power to heaters inside the specimen holders for high-temperature tests, and compressed-air vortex tubes quickly cool them down during thermomechanical cycling tests.

2.7.1 Heating

Heat is applied by electrical resistance cartridge heaters located inside the grips which fixture both ends of the specimens. This creats an even temperature distribution in the specimen because it is heated from both ends and it does not lose much heat in the middle because the air in the chamber is heated as well. Heat could have

also been applied by heating the air inside the thermal chamber or by heaters placed inside the specimens, but this method would have created much larger temperature gradients. The cartridge heaters are capable of heating the specimen grips and specimen from room temperature to the highest test temperature, 121°C (250°F) in less than two minutes. Since this is faster than the testing specifications require, they are not used at full power for this part of the heating cycle.

The heaters are controlled by the computer running the tests by relays. The output systems, both Labview and dSPACE, can output 10 VDC, but only a few milliamps. Thus, a multi-stage relay system was needed to control the heaters. This relay system also has thermal fuses inside the thermal chamber that will break if they exceed 240°C (460°F), which will cut power to all of the other heating relays. This was necessary because in previous tests, the heating relays have broken twice. When they failed they kept supplying power to the heaters. With these additional fuses and safety logic, in the event of failure the thermal chamber will only heat to 240°C before it shuts off completely. This makes the tests safe enough to be run unmanned, which is essential for days or week-long creep or thermomechanical cycling tests.

2.7.2 Cooling

To achieve ten-minute thermal cycles a powerful cooling system is needed for the thermal chamber. The aluminum grips bonded to the NiTi tubes in the adhesive tests require larger fixtures than just plain tubes. Fans were investigated for cooling, but preliminary tests indicated that these would not be fast enough, particularly in the last parts of the cooling cycle near room temperature. Compressed air vortex tubes are used instead. Like fans, the vortex tubes provide a large air flow rate

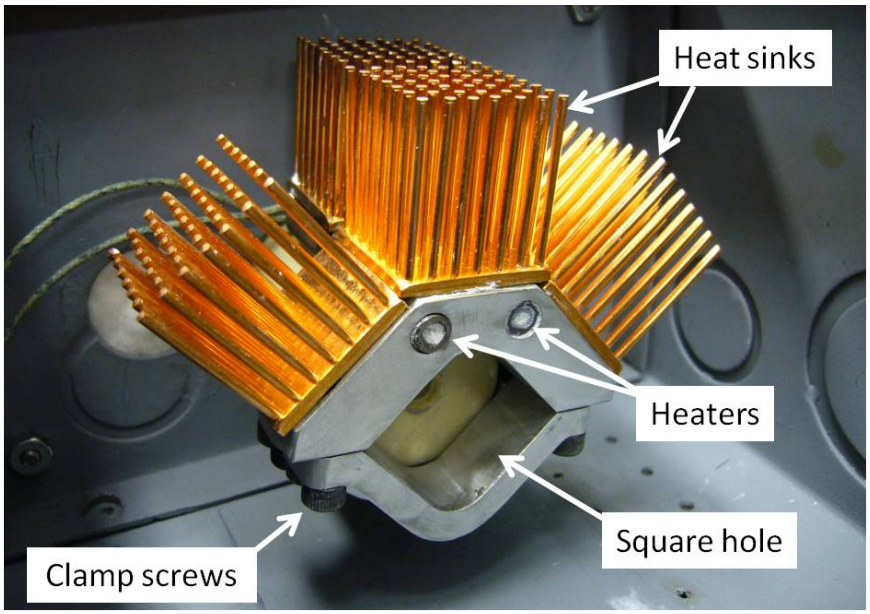

Figure 2.18: Redesigned square hole fixture for thermal cycling tests.

over the parts, but with air that is significantly colder than room temperature. This speeds the cooling, especially as the thermal chamber approaches room temperature. Also, the specimen grip holders were redesigned to have a smaller thermal mass and more convection than the old design. The old holders were designed for rigidity, so they were large steel V-grooves (seen in Figure 2.9(b)). The new holders are smaller, aluminum, and have heat sinks attached to them. Finite element analysis was done to find the minimum dimensions of the holders to still be able to transmit 500 in-lb of torque, as well as predict the thermal gradients and heating times that they would produce. Photographs of these new holders are shown in Figures 2.18 and 2.19.

Based on the capabilities of the available compressed air system, a 10 to 15 SCFM vortex tube was purchased from Streamtek Corporation, as well as six different vortex generators to be tested. The vortex tube and each of the generators was tested to

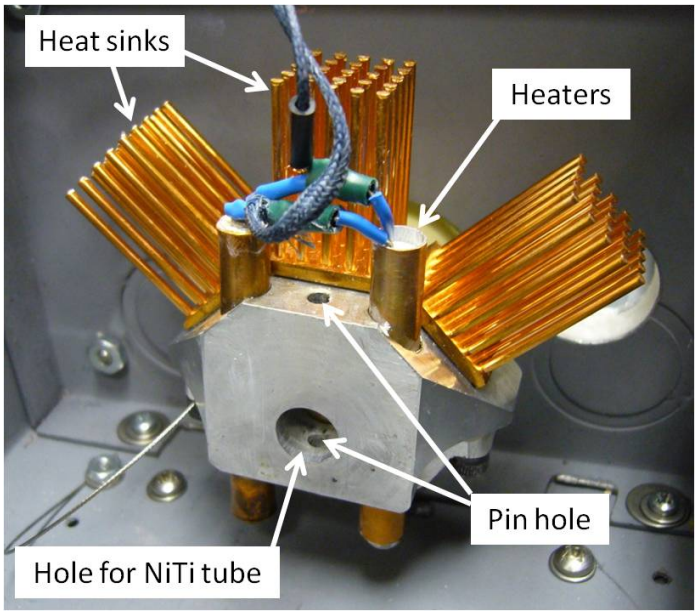

Figure 2.19: Redesigned pin grip fixture for thermal cycling tests.

assess which generator and settings on the vortex tube produced the fastest cooling. The cold air output was directed across the heat sinks on the holders, and the tests were started at the hottest test temperature, 121°C. Figure 2.20 show that the vortex tubes compare favorably against cooling fans. The test specimen was cooled from 121°C to 25°C (250°F to 77°F) in 215 seconds with the fastest vortex tube settings versus 520 seconds with the cooling fan, an improvement of about five minutes.

Each thermal cycle requires about seven minutes total, which allows about 200 per day and 1400 per week. The cycle time is divided as follows:

1. Two minutes for heating from 25°C to 121°C.

2. Thirty seconds dwell at 121°C to ensure all of bond line is properly heated.

3. Four minutes (a conservative estimate) for cooling back to 25°C.

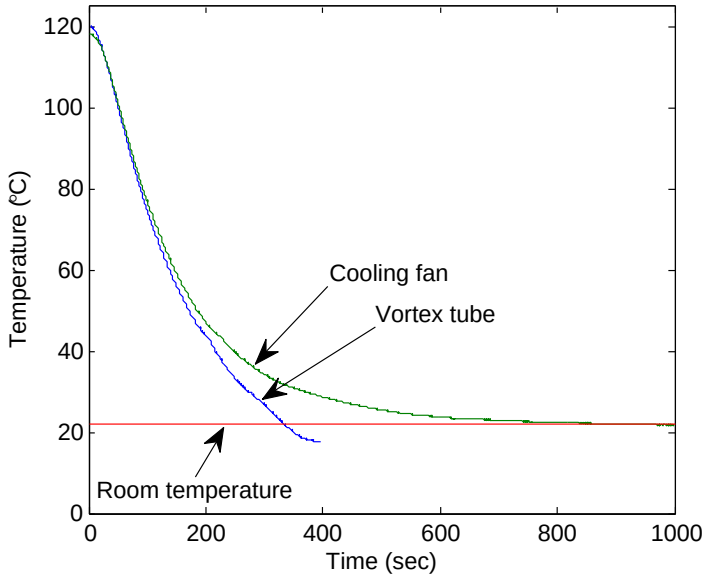

Figure 2.20: Test data for vortex tube and fan cooling.

4. Thirty seconds dwell at 25°C to let thermal gradients die out before beginning again.

2.7.3 Temperature Measurement and Control

In the heating phase of thermal cycling tests, the heaters are turned on at a fixed power until a certain temperature is reached. This is an effective way for heating quickly, but it is not accurate enough for maintaining a constant temperature for ultimate failure and creep tests. Temperature measurements are taken by two thermocouples mounted on either end of the specimens. For the adhesive specimens, one thermocouple is placed as close as possible to the bond line and the other is placed inside the free end of the NiTi tube, as shown in Figure 2.21. Placing the thermocouples at these points gives the best estimate of the temperature in the NiTi tube and adhesive bond. This was verified by both FEA thermal analysis and by comparing

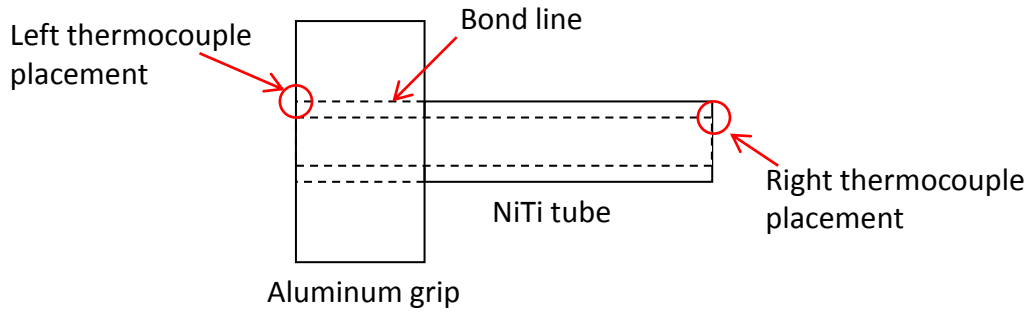

Figure 2.21: Placement of thermocouples on adhesive specimens.

these readings with that of a thermocouple embedded inside the adhesive bond of a trial specimen.

In order to control the heaters, a feedback control law was developed from a simplified approximation of the dynamics of the system. The temperature inside the specimen, the bonded aluminum grip, and the grip holders has a continuous distribution, but a two degree-of-freedom system was found to approximate it well enough. This system model is two masses connected together, where heat from the cartridge heaters is applied to one and the thermocouple is placed on the other. Heat transfers from the first mass to the second and from each mass to the ambient air. It was also necessary to introduce a feedback delay in the model of the left side to account for the time it takes the heat to diffuse through the system. The parameters of this model were tuned to fit data from characterization tests run with a trial specimen. An illustration of this model is shown in Figure 2.22 and the tuned parameters are in Table 2.1. The model is divided into a "left" and "right" side because the specimens have aluminum grips adhered to their left side and use pin grips on their right. The holders to fixture each side of these specimens in the torsional machine are also

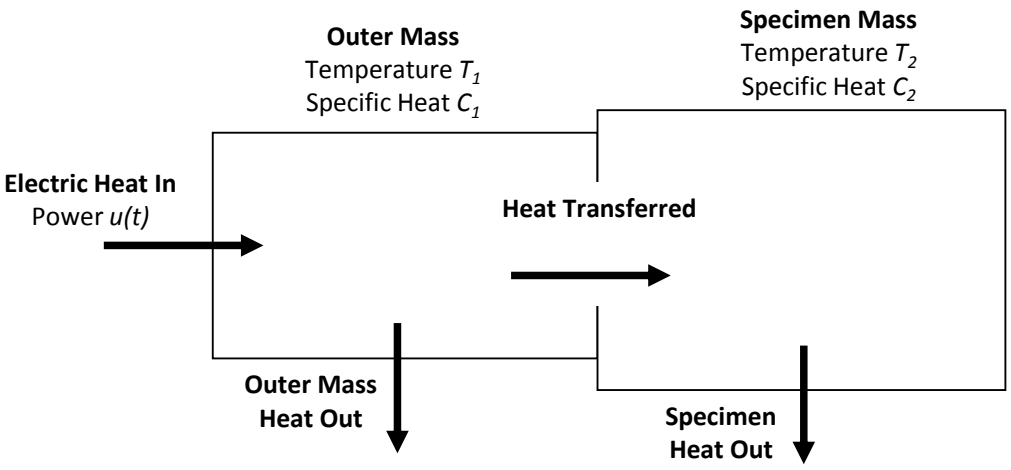

Figure 2.22: Two degree-of-freedom model of thermal chamber.

	Left Side (adhesive bond)	Right Side (pin grip)
Specific heat (J/°C)	98	43
Ratio of mass 2 to total mass	0.6	0.9
Conduction between masses (W/°C)	2.0	1.0
Heat lost to ambient (W/°C)	0.08	0.07
Feedback delay (sec)	3	0

Table 2.1: Thermal model parameters.

different. It can be noticed in Table 2.1 that the right side, which uses the pin grip, has a thermal mass less than half as large as the left side. In practice, the response of two sides is weakly coupled because heat can travel through the specimen between them, but in the model they are treated independently because the heat transfered by this coupling is small compared to the heat applied by the heaters.

The control law uses full-state feedback (the temperature of both masses in Figure 2.22) as well as the integral of the error between T_2 and the command input. The

temperature of the first mass, T_1, is estimated because it cannot be measured. To design the feedback gains, all poles of the closed loop system were placed at -0.05 on the complex plane, then the gains calculated with Ackerman's formula in MATLAB. This controller performed well when tested. When the command input was changed by 5°C it heated the system to within 1°C of the new reference in approximately two minutes, with no overshoot. The controller was able to compensate for both impulse and step disturbances.

To heat the ultimate failure and creep specimens to temperature, the heaters are turned on at a constant power until a cutoff temperature is reached, when they are turned off completely. This cutoff is usually set 10° to 20° below the desired final temperature. The temperature at the thermocouples keeps increasing for a little while after the heaters are turned off as the heat from right around the heaters disperses through the grips and specimen. When the thermocouple temperature stops increasing, which is usually within 5° of the desired final temperature, the state-space control is turned on to get exactly to the desired temperature. The feedback state-space controller is used for the rest of the test to maintain that temperature. Using the on/off heating for most of the heating and the feedback controller for the fine tuning allows quicker heating than if the feedback controller were used for all of it.

Chapter 3: JOINING RESULTS

Four joining methods were investigated in this research: ultrasonic soldering, laser welding, tungsten inert gas welding, and adhesives. All of these methods were found to produce viable, useful joints, and each had its strengths and weaknesses. A detailed description of how each method is performed and the results obtained from them is given in this chapter. Chapter 4 is a comprehensive comparison of these methods, including strengths, weaknesses, and applications each is suited for.

3.1 Ultrasonic Soldering

The first method discussed here is ultrasonic soldering (USS), a fluxless soldering process which has proven successful for soldering difficult to wet materials such as metals, ceramics and plastics [17]. In USS an ultrasonically vibrating soldering iron is inserted into pools of solder melted on a workpiece. The vibrations of the iron create cavitations in the liquid solder which implode, and the pressure waves created by these implosions break up the surface oxide layer allowing proper wetting of the workpiece. The pieces are then assembled and allowed to cool. This process is illustrated in Figure 3.1.

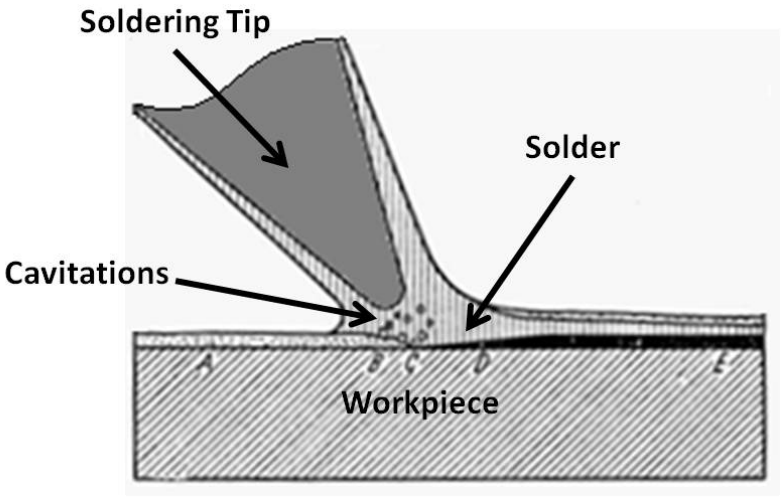

Figure 3.1: Illustration of USS process.

3.1.1 Specimen Design and Construction

Previous studies examined different material combinations to determine which one would yield the strongest joints with NiTi. Among 304 stainless steel, O1 tool steel and aluminum 2024 (Al 2024), aluminum formed the strongest soldered joints with NiTi [8]. A tube-and-socket joint was used to take advantage of the ability of a soldered joint to have a large contacting area. Butt joints are possible, but would be much weaker because of their smaller contacting area.

The specimens were NiTi tubes soldered into holes in Al 2024 blocks, with a 0.003" (0.08 mm) wide solder gap between the outside of the tube and the inside of the hole. The tube was soldered to blocks on both ends. The block on one end had a 0.381" (9.68 mm) diameter blind hole, 1/2" (12.7 mm) deep, while the block on the other end had a 0.381" (9.68 mm) diameter hole for 1/4" (6.35 mm), then a 1/2" diameter hole for the rest of the thickness of the block. Joints were only made with the part of

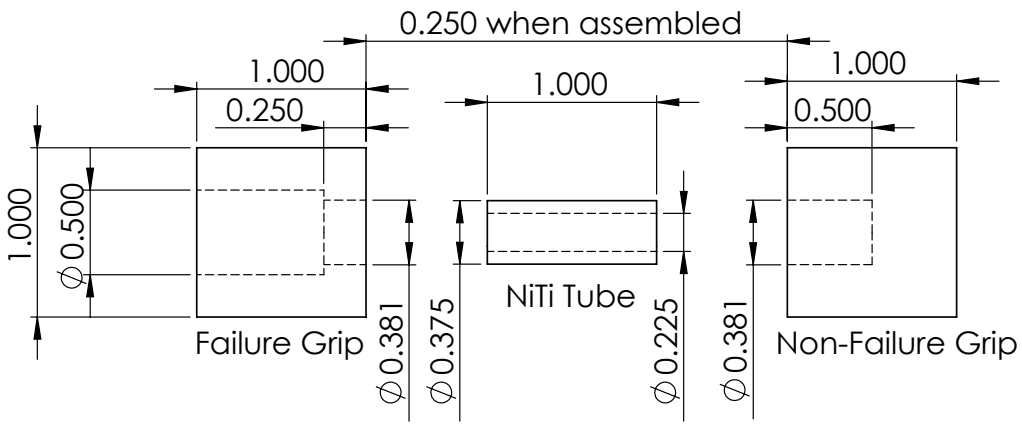

Figure 3.2: USS specimen geometry.

the holes that were 0.381" in diameter. The shallower joint in the second block was intended to fail first, and it did in all the tests. The NiTi tubes were 1" (25 mm) long, and when the specimens were assembled, the faces of the aluminum blocks were 1/4" (6.35 mm) apart. This geometry is illustrated in Figure 3.2. Five specimens were made for mechanical testing.

3.1.2 Mechanical Testing

For the ultimate failure tests, the specimens were fixtured in the torsional testing machine (Figure 2.1) with square hole couplers. On one side, these fixed the square aluminum blocks of the specimens rigidly, and on the other side were attached to the main shaft of the machine which rotated. Deflection was applied at a rate of approximately 0.5 °/second, and was measured by the rotary encoder on the main shaft of the machine. The breaking torques are listed in Table 3.1 and the torque versus angle plots are shown in Figure 3.3. In the table of ultimate torques, the C_v

value is the standard deviation divided by the mean, which gives an indication of how large the variation is compared to the average.

The shear strength of the soldered joints was calculated from the breaking torque by assuming that the solder was only loaded in shear, and it uniformly transmitted torque from the NiTi tube to the aluminum block. Shear stress, τ, can be calculated from force, F, by

$$\tau = \frac{F}{A} \tag{3.1}$$

where A is the area the force is applied over. Torque, T is created from a force acting a radius r away from the axis of rotation by

$$T = F \times r \tag{3.2}$$

and the area of the soldered joint is the circumference of the NiTi tube times the bond depth, d, which gives

$$A = 2 \times \pi \times r \times d. \tag{3.3}$$

Specimen	Ultimate Torque (in-lb)[N-m]	Shear Strength (ksi) [MPa]
1	282 [31.9]	5.11 [35.2]
2	288 [32.5]	5.22 [35.9]
3	284 [32.1]	5.14 [35.4]
4	297 [33.6]	5.38 [37.1]
5	327 [37.0]	5.92 [40.8]
Average	296 [33.4]	5.35 [36.9]
Standard Deviation	18.5 [2.09]	0.33 [2.3]
C_v	6.2%	

Table 3.1: Ultimate torque of USS specimens.

Combining (3.1) through (3.3), one gets

$$\tau = \frac{T}{2 \times \pi \times d \times r^2} \tag{3.4}$$

which was used to calculate the stresses in Table 3.1. In the calculations $r = 0.189$" (4.8 mm) which is the mean radius of the solder, and $d = 0.25$" (6.35 mm). A more detailed model of the stress in the soldered joints, which also accounts for residual stress from the cooling of the joints, was developed by Hahnlen [10].

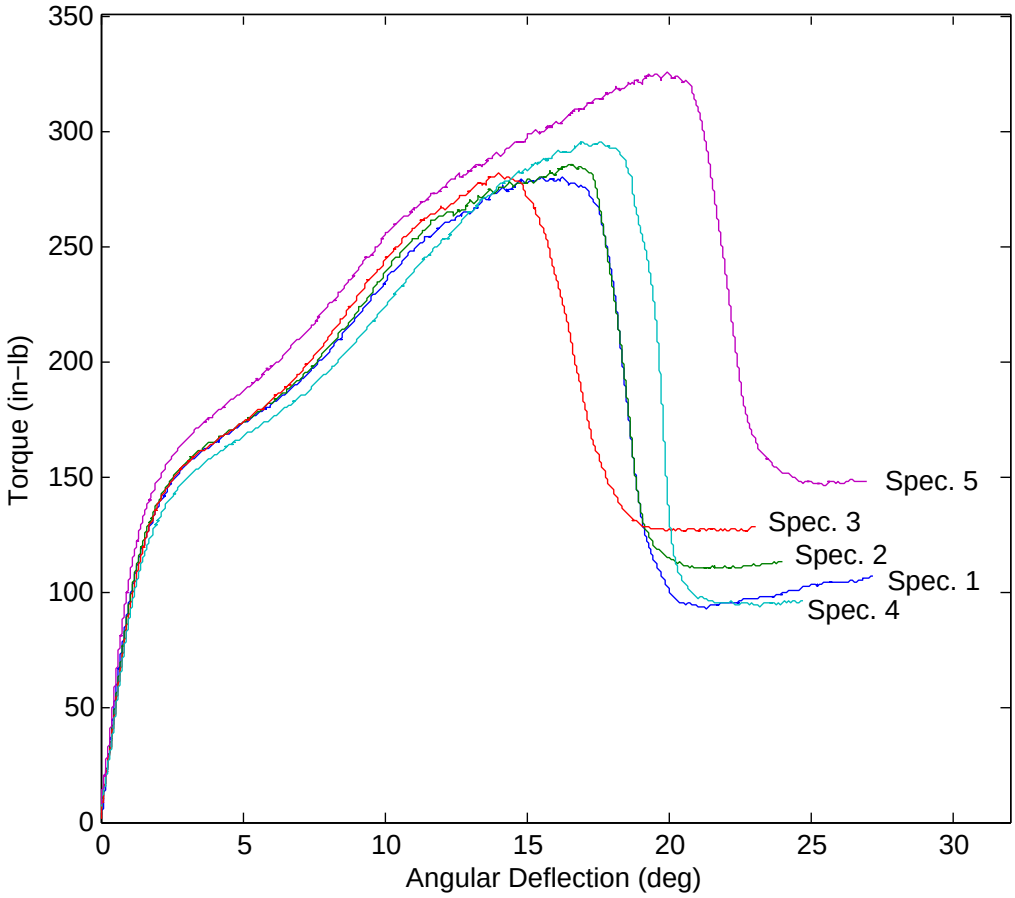

Figure 3.3: Torque vs angle plot from USS tests.

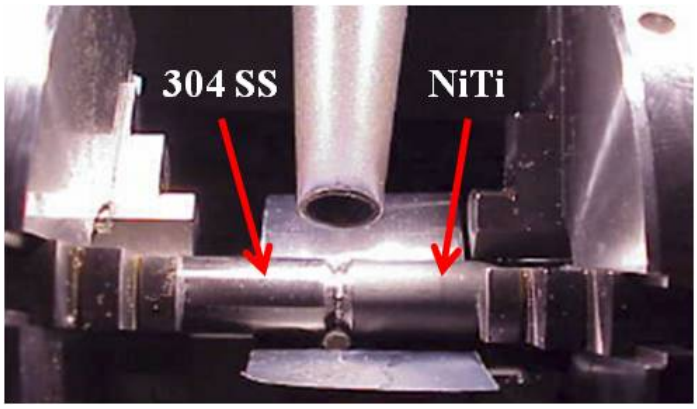

Figure 3.4: Laser welding process.

3.2 Laser Welding

Laser and tungsten inert gas (TIG) welding were the two fusion welding process used to join NiTi tubes to 304 stainless steel (304 SS) tubes. Fusion joining methods offer the advantage of higher strength compared with soldered or adhesive joints, especially at elevated temperatures. The results from laser welding are presented first, then the results from TIG welding in Section 3.3.

3.2.1 Specimen Design and Construction

All of the laser welded joints were made with a neodymium-doped yttrium aluminum garnet (Nd:YAG) laser with argon as a shielding gas to prevent atmospheric contamination. The parameters used to make each joint are listed in Table 3.2. The specimens were held in a welding lathe and rotated while the laser remained stationary. A photograph of this process is shown in Figure 3.4.

Thick Walled

The penetration of the pilot welds was limited to about 0.015" (0.38 mm), so in order to weld thicker walled tubes multiple weld passes were needed. A bevel joint geometry was used to test forming a deep joint with multiple weld passes. The specimens had 45° bevels cut out of the ends of NiTi and 304 SS tubes, and Ni wire was used as filler material. This geometry is illustrated in Figure 3.5(a), and a photograph of completed specimens is shown in Figure 3.5(b). This welding process is similar to large-scale pipe welding, and can have a nearly indefinite weld depth, which compensates for the relatively shallow single-pass penetration available from laser welding.

The NiTi and 304 SS tubes had an outer diameter of 0.375" (9.5 mm) and wall thicknesses of 0.065" (1.65 mm). The first, root passes used 0.010" (0.25 mm) diameter nickel wire for filler metal while the fill passes used 0.020" (0.51 mm) diameter wire. The laser spot size was set at 0.4 mm for the root passes and 0.75 mm for fill passes. Pulse frequency for each pass was fixed at 5 pulses per second. These and other welding parameters are shown in Table 3.2.

Thin Walled

A second geometry was used to investigate the strength of a single full-penetration weld pass. A butt joint configuration was used. These specimens were made from tubes with the same, 0.375" outer diameter as the thick-walled joints, but with a wall thickness of only 0.015" (0.381 mm). The inner diameter of the NiTi tubes was enlarged via electro-discharge machining (EDM). The Ni filler was placed with custom

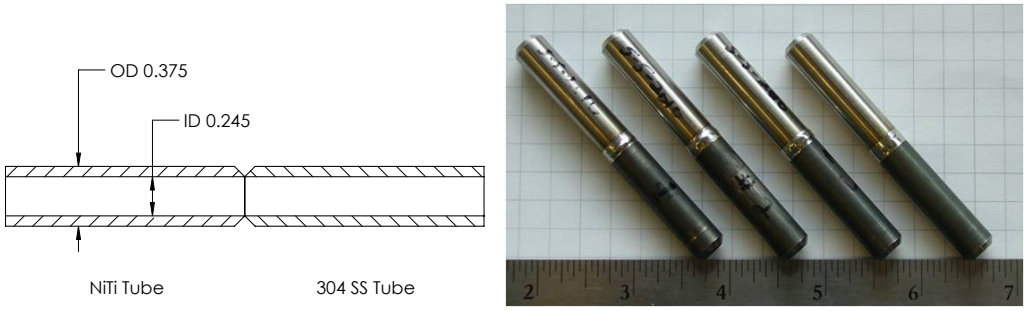

(a) Geometry of specimen. (b) Photograph of specimens

Figure 3.5: Thick walled laser weld specimens.

machined Ni unions inserted between the tubes prior to welding. This geometry is shown in Figure 3.6(a).

Five thin-walled samples were made. Four were tested for torsional strength and the fifth was sectioned and used for optical microscopy in order to observe the weld penetration and the resulting fusion zones and HAZ. While welding each specimen, the spot size, peak power, and pulse frequency were fixed at 0.7 mm, 1.1 kW, and 1.3 pps, respectively. The pulse energy was varied by adjusting pulse duration. All of these parameters are listed in Table 3.2. Thin-walled samples 3, 4, and 5 were made with identical parameters. It can be seen in Figure 3.6(b) that the first specimen is discolored near the weld line. This indicates excessive heating, so the pulse energy was decreased for the subsequent specimens.

3.2.2 Mechanical Testing

One of the thick-walled specimens and four of the thin-walled specimens were tested in torsion until failure. Deflection was applied at approximately 0.5 °/second while torque and the angle of the main shaft of the torsional machine were recorded.

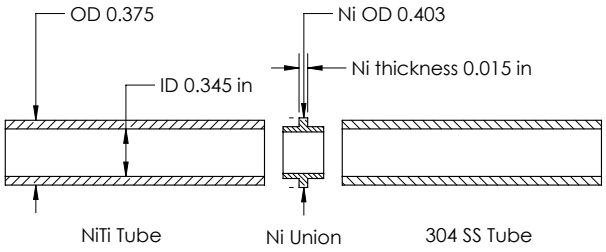

(a) Geometry of specimen.

(b) Photograph of specimens

Figure 3.6: Thick walled laser weld specimens.

Type	Specimen	Spot Size [mm]	Pulse Frequency [pps]	Peak Power [kW]	Pulse Duration [ms]	Pulse Energy [J]
Thin-Walled	1	0.70	1.3	1.25	14.0	17.5
	2	0.70	1.3	1.15	13.0	15.0
	3	0.70	1.3	1.10	13.0	14.3
	4	0.70	1.3	1.10	13.0	14.3
	5	0.70	1.3	1.10	13.0	14.3
Thick-Walled	Root	0.40	5.0	0.52	3.4	1.8
	Fill	0.75	5.0	1.00	13.0	13.0

Table 3.2: Laser welding parameters.

The breaking torques and the shear strengths of the laser welded specimens are listed in Table 3.3. Plots of the mechanical behavior of the thick and thin-walled specimens can be seen in Figures 3.7 and 3.8. Specimen number 3 had pin hole defects on the weld line, which caused its failure torque to be much lower than the other thin-walled specimens. Because of this, it was omitted from the average calculations, so the average reflects the strength of laser welds that have no obvious defects and which pass visual inspection.

The shear strength of the welds was calculated from the breaking torque by

$$\tau = \frac{T \times r_o}{J} \tag{3.5}$$

where τ is the shear strength, T is the breaking torque, and J is the polar moment of inertia of the cross section, given by

$$J = \frac{\pi}{2}\left(r_o^4 - r_i^4\right) \tag{3.6}$$

where r_o is the outer radius of the tube, and r_i is the inner radius of the tube. For all of these tubes $r_o = 0.1875$" (4.76 mm). For the thin-walled tubes $r_i = 0.1725$" (4.38 mm) and for the thick-walled tubes $r_i = 0.1225$" (3.11 mm).

The thick-walled specimens had about a 25% lower ultimate shear stress than the thin-walled specimens. This was likely due to voids in the weld which were observed when the other thick-walled specimens were sectioned. These voids were probably caused by contamination on the base metals prior to welding, so they can be prevented by better pre-weld cleaning.

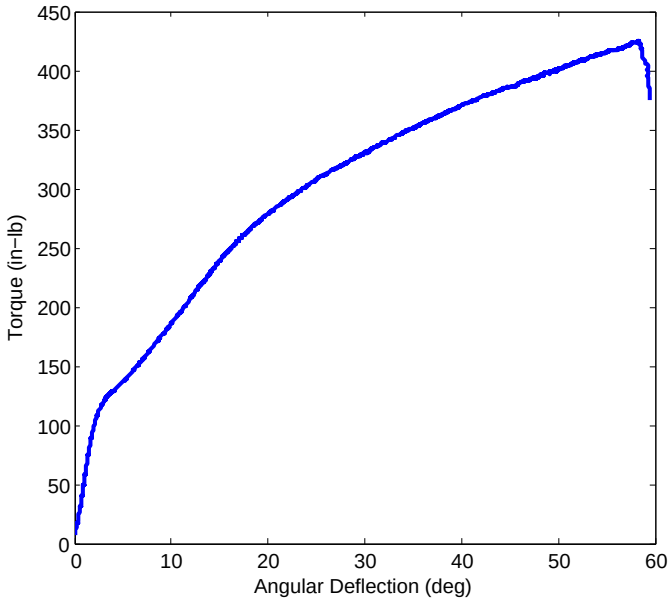

Figure 3.7: Torque vs angle plot for thick walled laser specimen.

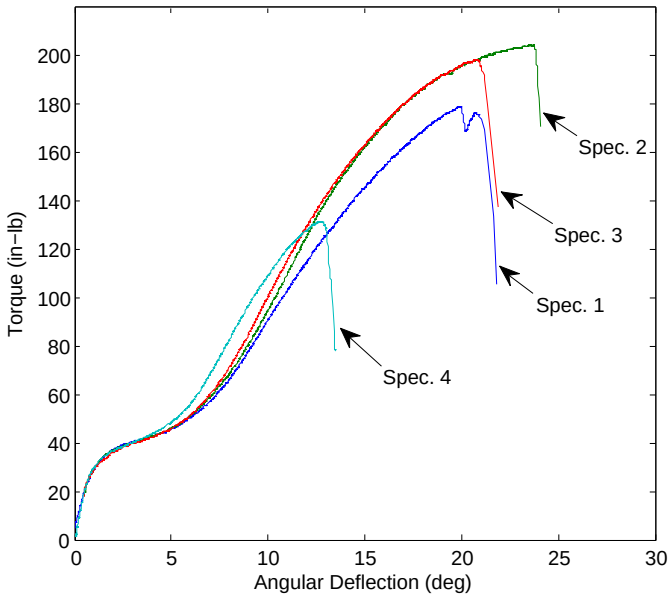

Figure 3.8: Torque vs angle plot for thin walled laser specimens.

Sample	Ultimate Torque (in-lb) [N-m]	Ultimate Shear Stress (ksi) [MPa]
Thick-Walled	422 [48.0]	50.2 [346]
Thin-Walled 1	178 [20.3]	61.3 [423]
Thin-Walled 2	204 [23.2]	69.7 [481]
Thin-Walled 3	132 [15.0]	45.3 [312]
Thin-Walled 4	197 [22.5]	67.6 [467]
Thin-Walled Average[a]	193 [22.0]	66.3 [457]
Standard Deviation[a]	13 [1.5]	4.4 [30]
C_v		7.0%

[a] Average and standard deviation calculated with specimens 1, 2, and 4

Table 3.3: Breaking torques and shear strengths of laser welded specimens.

The characteristic mechanical behavior of NiTi can be observed in the torque versus angle plots in Figures 3.7 and 3.8. At low stresses and temperatures shape-memory NiTi components behave linear-elastically because the NiTi in them is in the twinned martensite phase. As the stress is increased, the NiTi piece begins to detwin. The material is less stiff while detwinning than in its initial linear-elastic region, which can be seen in mechanical behavior plots as a decrease in the torque/angle slope or stress/strain slope. The NiTi in the component will detwin over a range of strain, then once it is fully detwinned the material will behave linear-elastically again, which can be seen as an increase in the torque/angle slope.

When NiTi tubes are loaded in torsion the detwinning region in stress/strain plots has a higher slope than in plots made from tension tests [16]. This is due to the fact that there is a range of stresses across the cross section of the tube instead of a uniform stress like there is in a tensile test. When the material on the outside of the tube reaches the critical detwinning start stress, the material on the inside is at a

	Torques		Shear Stresses	
Sample	Critical Start (in-lb) [N-m]	Critical Finish (in-lb) [N-m]	Critical Start (ksi) [MPa]	Critical Finish (ksi) [MPa]
Thin-Walled 1	36.2 [4.12]	49.6 [5.64]	12.3 [85.0]	16.9 [116]
Thin-Walled 2	35.4 [4.03]	49.0 [5.57]	12.1 [83.2]	16.7 [115]
Thin-Walled 3	34.5 [3.93]	49.8 [5.67]	11.8 [81.1]	17.0 [117]
Thin-Walled 4	33.7 [3.84]	48.8 [5.55]	11.5 [79.2]	16.6 [115]
Thin-Walled Avg.	35.0 [3.98]	49.2 [5.61]	11.9 [82.1]	16.8 [116]
Thick-Walled 4	115 [13.1]	unclear	13.6 [93.9]	unclear

Table 3.4: Critical detwinning start and finish stresses in laser welded specimens.

lower stress and is still linear-elastic. Then, when the material on the inside of the tube is detwinning, the material on the outside may have finished detwinning and entered the second linear-elastic region.

Another effect that can be seen in the mechanical behavior plots is the yielding of the 304 SS tubes. The 304 SS tubes were annealed prior to welding, which decreased their yield strength, so they plastically deformed during the tests. This made it impossible to find the end of detwinning for the thick-walled laser welded specimen because it was confounded with the onset of yielding in the 304 SS tube. All of the other critical start and finish torques for detwinning were calculated from the data in Figures 3.7 and 3.8, and were used to calculate critical stresses for detwinning. These torques and stresses are listed in Table 3.4.

3.2.3 Sectioning and Hardness Mapping

These joints were sectioned for hardness mapping, and scanning electron microscopy by Hahnlen. After sectioning, the joints were mounted in an epoxy matrix and polished. More optical and scanning electron microscopy studies were performed than are detailed in this thesis [9].

Hardness maps were created by making an array of indents with a 25 gram load with a diamond indenter. The indents were spaced 70 μm apart in both the axial and radial directions on the thin-walled sample and 130 μm apart on the thick-walled sample. These hardness maps can be seen in Figures 3.9 and 3.10. An affected zone can be clearly seen in the thick-walled hardness map as a line of increased hardness bordering the weld pool. The resolution of the thin-walled hardness map was not fine enough to observe an affected zone, so individual indents were taken with a 50 gram load at manually selected points of interest. Some of these additional indentations can be seen in Figure 3.11.

These results indicated that the affected zone produced from laser welding was indeed small. It was 7.9 and 21.9 μm (3.11 and 8.62 $\times 10^{-4}$ in) wide with a maximum hardness of 929 and 801 Vickers hardness in the thin-walled and thick-walled specimens, respectively. The NiTi farther away from the weld line had no increase in hardness from its pre-welded value of about 350 HV, which is typical for NiTi [1].

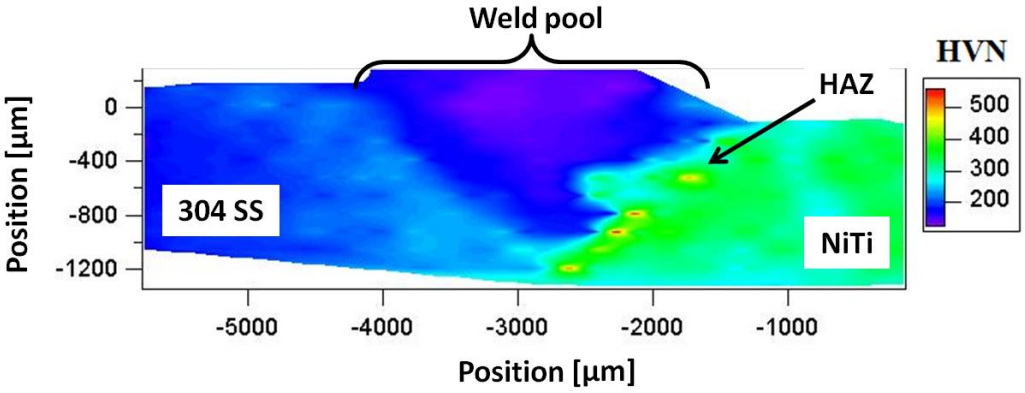

Figure 3.9: Hardness map of thick-walled laser welded joint.

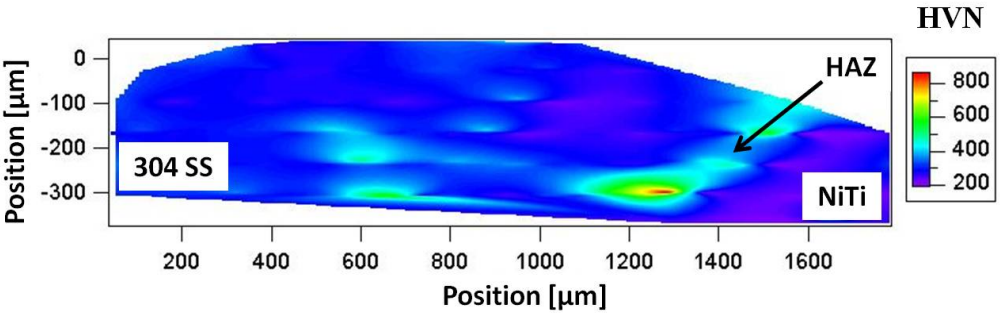

Figure 3.10: Hardness map of thin-walled laser welded joint.

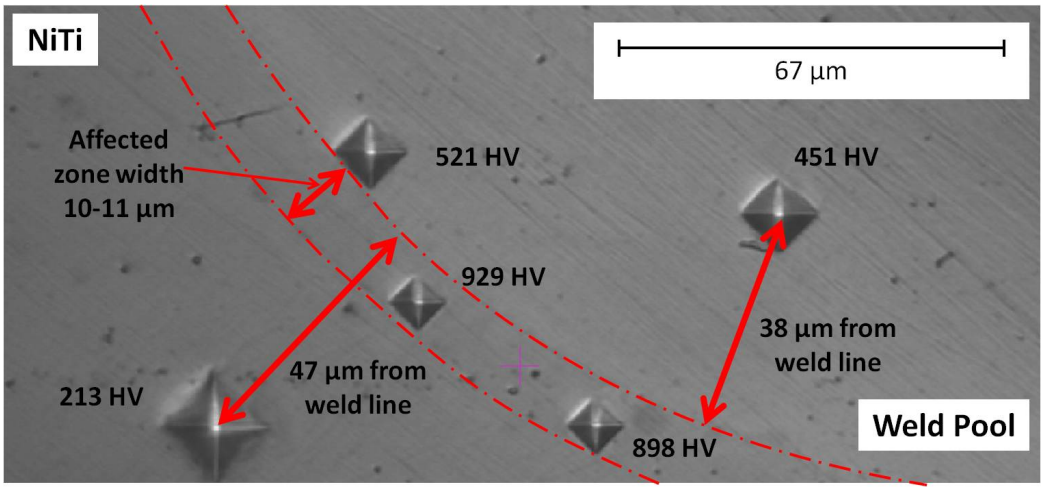

Figure 3.11: Individual hardness indents in thin-walled laser weld.

3.3 Tungsten Inert Gas Welding

The second fusion welding method presented in this thesis is tungsten inert gas (TIG) welding. This process uses an electric arc from a non-consumable tungsten electrode to melt the workpieces while an inert shielding gas, generally argon, protects the weld from oxidation. It is a common process for fabricating and repairing metal structures, so the necessary equipment is more widespread in industry than laser welding equipment.

TIG is a higher power process than laser welding which means that it can create deeper weld penetration, but it also creates a larger heat affected zone. Joints of the same depth can be made in fewer passes with TIG than laser welding, but there will be more loss of the shape memory effect and cold work in NiTi workpieces due to the larger affected zone.

The welds in this study were created via orbital TIG welding where two tubes are held in a clamp while the electrode circles their circumference. It is an automated process so variables such as the speed of travel and gap between the electrode and workpiece can be precisely controlled, producing more consistent joints than manual TIG welding.

3.3.1 Specimen Design and Construction

NiTi and 304 SS tubes were welded together in a butt joint configuration. The outer diameters of the tubes were 0.375" (9.5 mm) and their wall thicknesses were left as-received, which was 0.075" (1.91 mm) and 0.065 (1.65 mm) for the NiTi and 304 SS tubes, respectively. Nickel filler metal was placed via pre-made Ni unions,

similar to the thin-walled laser welds. Overall, the wall thicknesses were similar to the thick-walled laser welds. This geometry is illustrated in Figure 3.12(a).

The welds were made with a M9-750 weld head connected to an AMI M307 power supply. Before the tubes were welded, the oxide layer on the outside of the tubes was filed off with a tungsten carbide file, and on the inside of the tubes with an inner diameter scraper. The welding electrode had a diameter of 1/16" (1.6 mm), a 0.010" (0.25 mm) wide flat, and an included angle of 22° for specimens 1 and 2, and 30° for 3 and 4. The arc gap between the tip of the electrode and the workpieces was 0.045" (1.1 mm). A photograph of this setup is shown in Figure 3.13. The primary and background electric pulse duty cycle was 0.19. The background current was 21.3 A, while the primary current was reduced every 90° through the orbit from 70.8 A at the beginning to 53.1 A at the end. This created an even heating in the base metals. A single orbit was conducted, which took 20 seconds. A 20 second pre and post-weld argon gas purge was also used to prevent atmospheric contamination. These parameters were selected by Steve Manring of the Edison Welding Institute where these welds were made, based off of his prior experience welding 304 SS tubes. A photograph of a completed specimen is shown in Figure 3.12(b).

3.3.2 Mechanical Tests

Two out of the four specimens made were tested in torsion until failure. They were fixtured with pin holes drilled radially through the tubes, 0.6" on either side of the weld line. Their breaking torques are listed in Table 3.5 and their mechanical behavior is plotted in Figure 3.14.

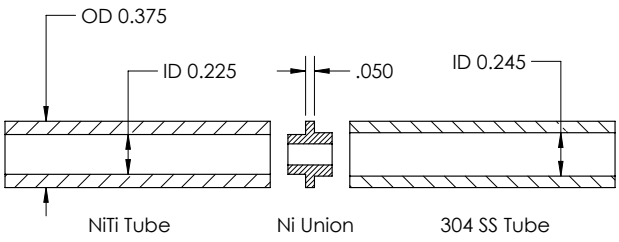

(a) Geometry of TIG welded specimens.

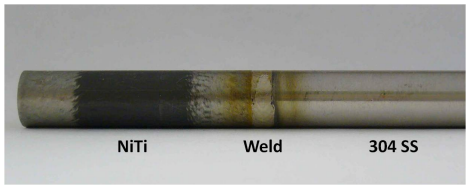

(b) Photograph of a TIG welded specimen.

Figure 3.12: TIG welded specimens.

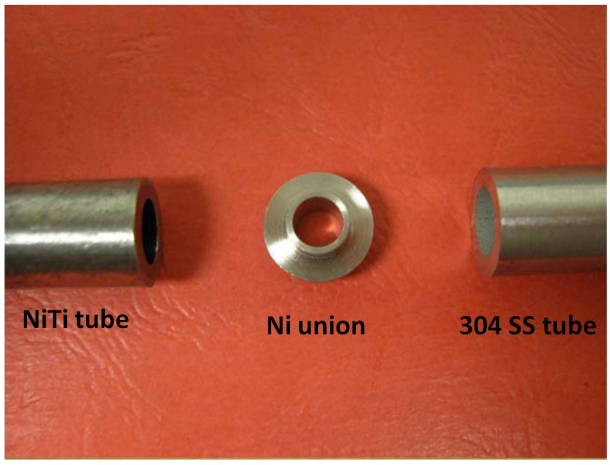

(a) NiTi and 304 SS tubes prior to welding

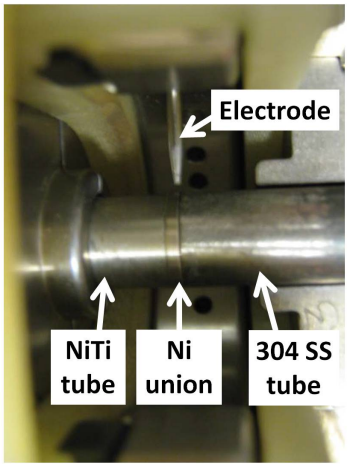

(b) NiTi and 304 SS tubes in orbital TIG welder.

Figure 3.13: TIG welding process.

Specimen	Breaking Torque (in-lb) [N-m]
1	458 [52.1]
2	448 [51.0]
Average	453 [51.6]
Std. Dev.	7 [1]
C_v	1.6%

Table 3.5: TIG welded specimens' breaking torque.

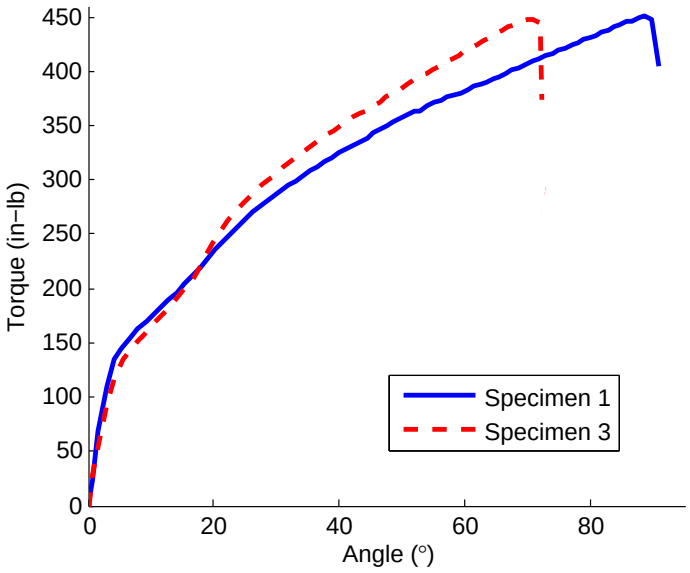

Figure 3.14: Torque vs angle plot of TIG welded specimens.

Calculating the shear strength of the welds from the breaking torque was not as straightforward as the laser welds because the TIG welds did not have full penetration through the walls of the tubes. This can be seen in the micrograph in Figure 3.16 which shows that the weld only penetrates through about 2/3 of the wall thickness. Below the maximum weld penetration there is a region that filled by molten weld metal via capillary action, but the base metals next to it were left unmelted. This may act as a brazing joint, which may have shared shear stress with the welded joint during the mechanical tests. Thus, exactly how much shear stress was on the welded joint when the specimen failed cannot be known. However, a range can be put on it by making different assumptions about this possibly brazed joint.

The shear strength of the TIG welded joints was calculated the same way as for the laser welded joints, by (3.5), except that the variable r_i is uncertain, so the strength

	Ultimate Shear Strength τ (ksi) [MPa]		
	Case 1	Case 2	Case 3
Specimen	Weld r_i	NiTi r_i	Ni r_i
1	60.8 [419]	50.8 [350]	46.0 [317]
3	59.5 [410]	49.7 [343]	45.0 [310]
Average	60.2 [415]	50.3 [347]	45.5 [314]

Table 3.6: Ultimate shear strength range of TIG welded specimens.

was calculated based on three different assumptions about it. The first assumption was that the area below the weld transmitted no shear stress, so r_i is the radius of the bottom of the weld penetration, 0.135" (3.44 mm). The second assumption was that this possible brazed joint transmitted shear stress through the butt end of the NiTi tube to the Ni union and 304 SS tube. The r_i used was that of the NiTi tube, 0.113" (2.86 mm). This also gives the shear stress in the NiTi tube. The third assumption is that the brazed joint transmitted shear stress to the Ni union, and did not fail before the weld failed. The r_i for this case was 0.083" (2.10 mm). The shear strengths calculated with each of these assumptions are shown in Table 3.6. It can be seen that the TIG welds had a shear strength between 45 and 60 ksi (315 and 415 MPa).

The mechanical behavior of the TIG welded specimens was compared with unwelded base metals to see what effect welding had on it. A NiTi tube and a 304 SS tube with the same inner and outer diameters as the tubes in the welded specimens were tested in torsion. They were fixtured with pins 1.2" (30 mm) apart as the welded specimens were, but their measured deflection was halved to simulate a 0.6" (15 mm) long specimen fixtured by a pin on one end and rigidly on the other, which is similar to how each base metal was loaded in the welded specimen tests. This accurately

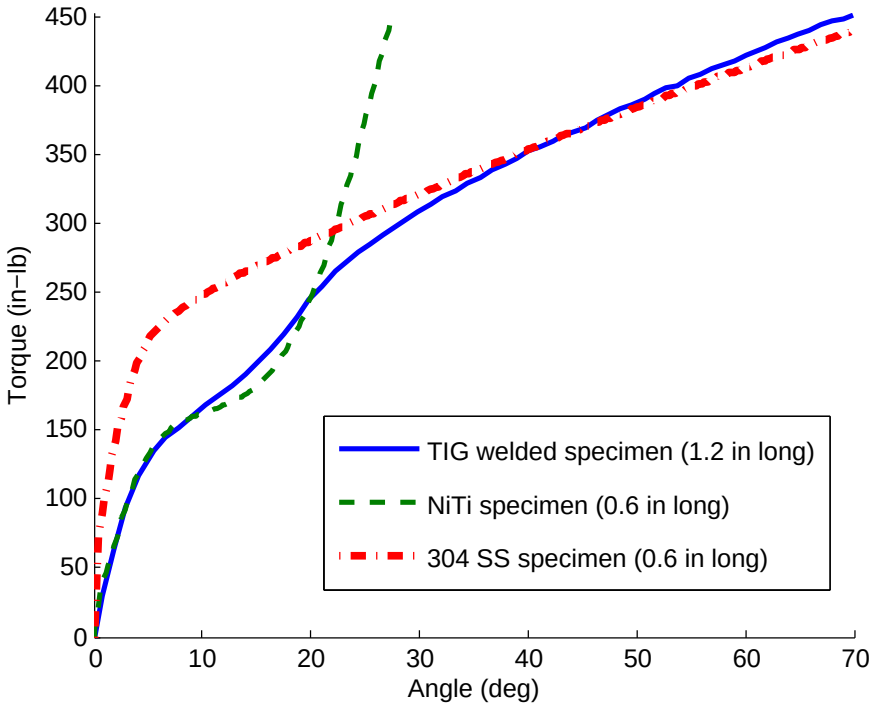

Figure 3.15: Mechanical behavior of welded specimen and unwelded base metals.

showed how much of the deflection in the welded specimen was from each base metal. A plot of the torque versus angle measured in these tests is shown in Figure 3.15.

3.3.3 Sectioning and Optical Microscopy

Hahnlen sectioned several TIG welded specimens, mounted them in an epoxy matrix, and polished them like the laser welded specimens. These were used for optical microscopy, hardness mapping, and scanning electron microscopy. A photograph of the sectioned weld is shown in Figure 3.16. In it the affected zone is clearly visible, as well as the weld penetration, capillary region, and several cracks. The strength of the two mechanically tested specimens was consistent, so it is likely that those either

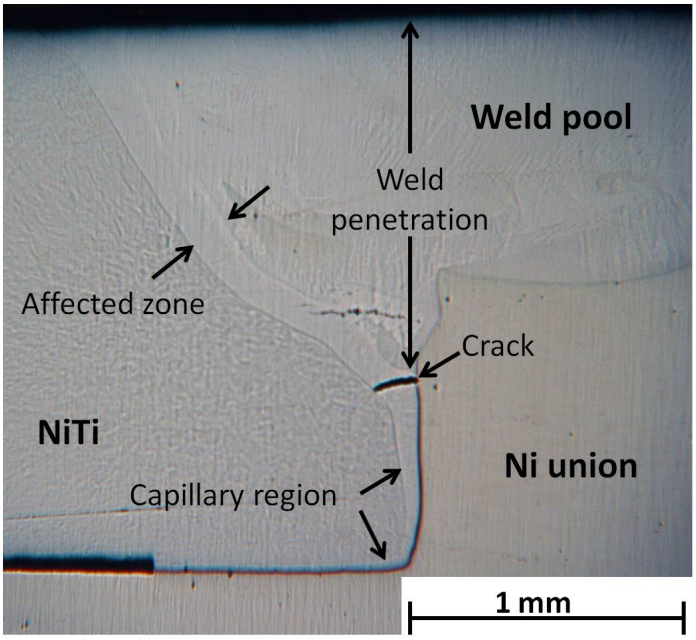

Figure 3.16: Penetration of TIG weld.

did not have such cracks, of it they did, the cracks did not significantly affect their strength. More variation in strength would be expected if the cracks were significant.

3.3.4 Hardness Mapping

A hardness map was made from the sectioned specimen with a 25 gram load on a diamond indenter. The indents were spaced 100 μm apart in both directions. The affected zone was larger in the TIG weld than the laser weld, so it was clearly visible on the initial hardness map, shown in Figure 3.17. This affected zone was 125 μm (0.003") wide with a maximum hardness of 817 HV. However, like the laser welded specimens, the hardness of the NiTi returns to normal, unwelded, levels immediately outside of this affected zone. This indicates that any loss of cold work or shape memory effect is limited to this narrow region.

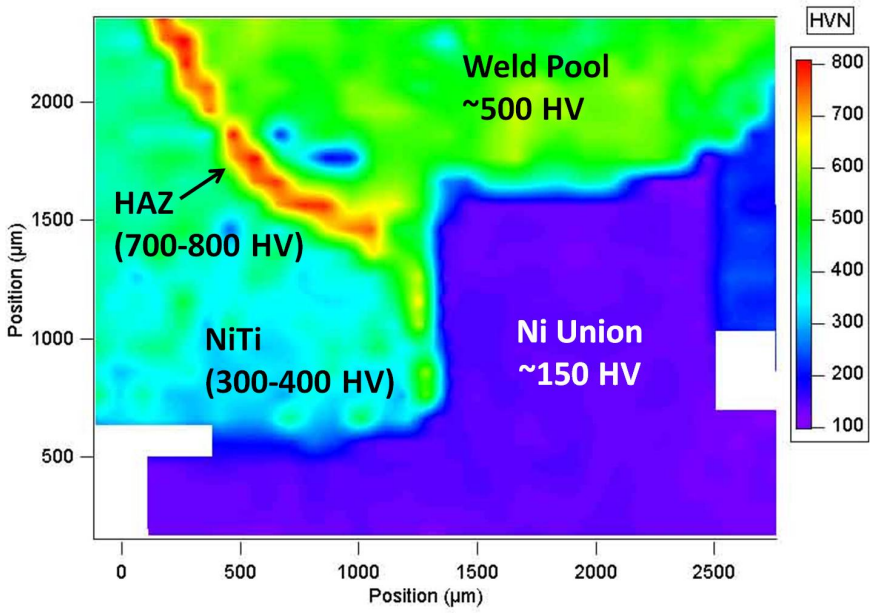

Figure 3.17: Hardness map of TIG welded joint.

More information on the sectioning, optical microscopy and hardness mapping can be found in the journal paper on this research [7].

3.3.5 Demonstration Actuator

Two demonstration actuators were constructed with NiTi tubes TIG welded to 304 SS tubes on either end. The NiTi tubes had been previously trained by the Boeing Company to have a two way shape memory effect where they twisted in one direction when heated and returned when cooled. The 304 SS tube on one end of the NiTi was held rigidly while the tube welded to the other end was supported with a ball bearing so that it was free to rotate. A gear was attached to this stainless steel tube which meshed with a smaller gear, which was connected to a pulley with a weight suspended from it. Thus, when the NiTi tube rotated, it turned the gears which turned the pulley

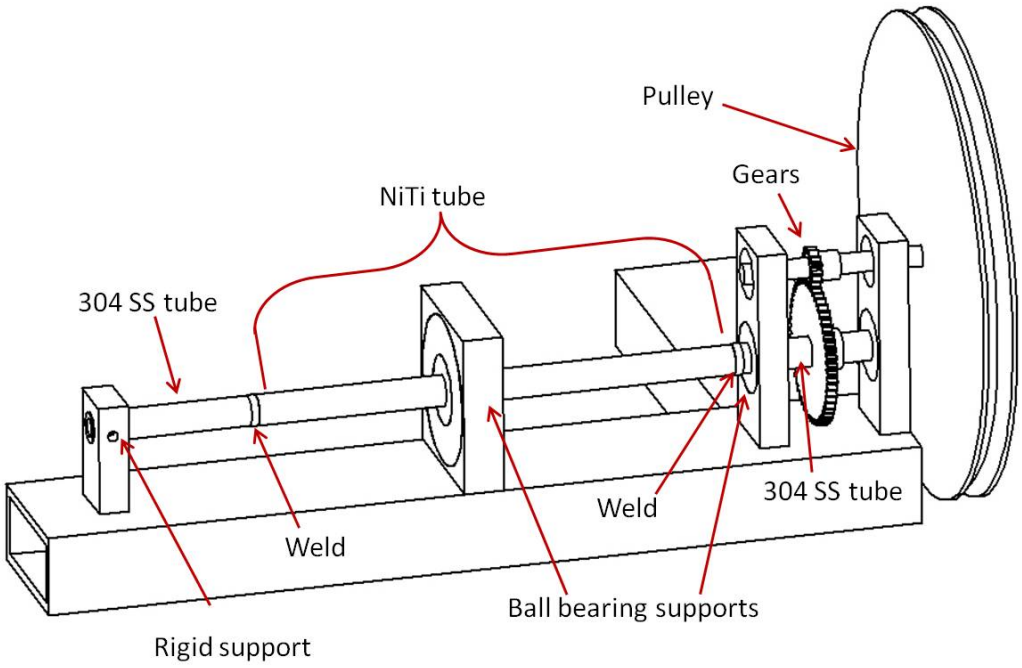

Figure 3.18: Drawing of demonstration actuator.

which lifted the weight. This design is illustrated in Figure 3.18, and a photograph of one of the completed demonstration actuators is shown in Figure 3.19.

The suspended weight applies 60 in-lb (6.8 N-m) of torque to the NiTi tube which is much less than it and the welds can withstand. This gives a large margin of safety between the breaking torque and the operational torque because the strength of these joints in cyclic loading is not yet known.

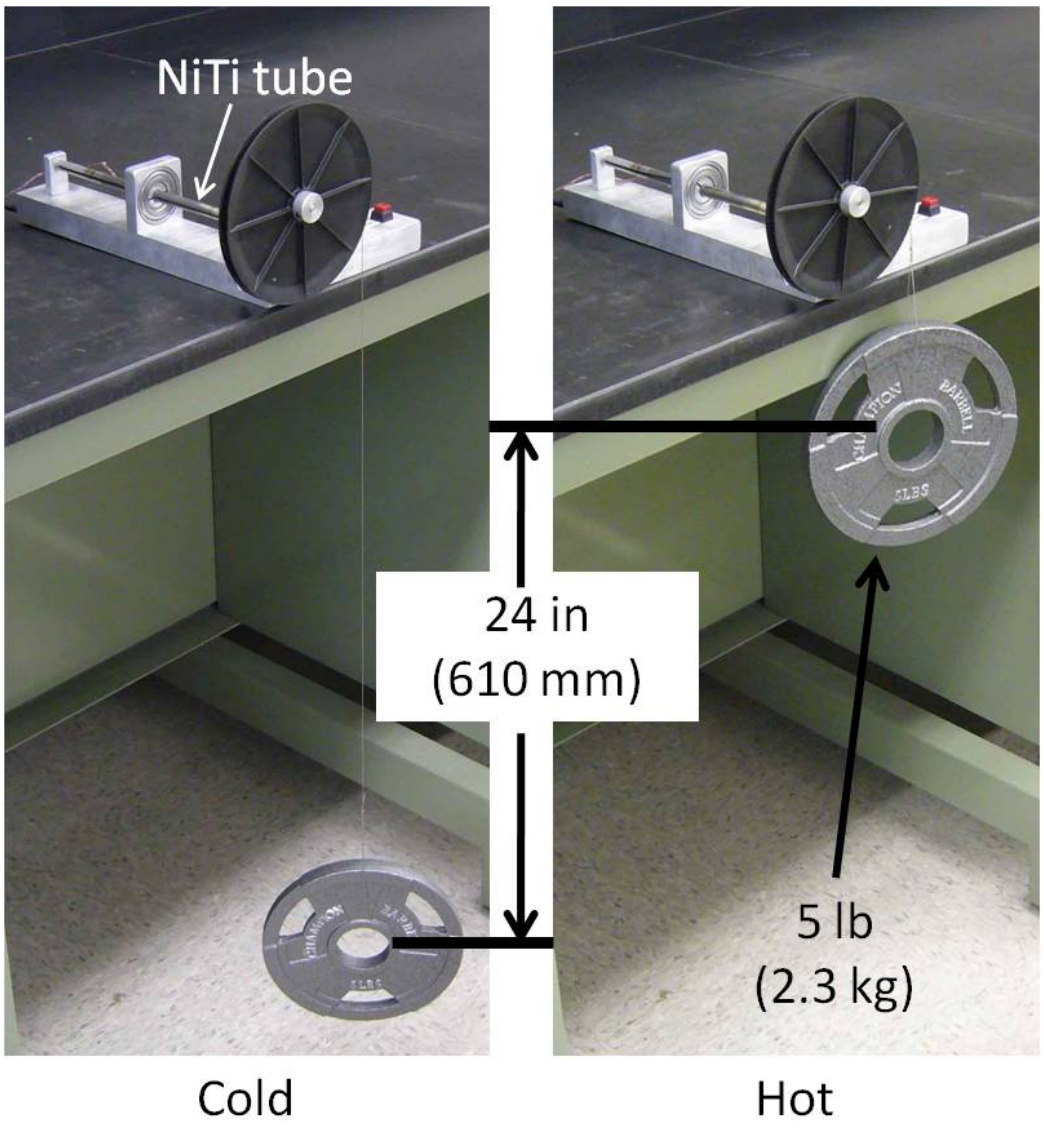

Figure 3.19: Photograph of demonstration actuator.

3.3.6 Future Work

This initial study of TIG welding indicated that viable joints can be made between NiTi and 304 SS. The next step of this study will be to investigate how strong they can be made. Several parameters have been identified which will be varied in the next trial. Specimens will be constructed with three different levels of each of these parameters. These are:

- Ni union width. The Ni union was 0.050" (1.3 mm) wide between the NiTi and 304 SS tubes in this first trial. The levels for the next trial will be 1: thinner than the current design, 2: the same as the current design, and 3: thicker than the current design.

- Ni union height. The outer diameter of the Ni union was flush with the outside of the tubes. The levels for the next trial will be 1: the same as the current design, 2: slightly larger than the outer diameter of the tubes, and 3: much larger than the outer diameter of the tubes.

- Pre-heat. Before the welding pass, a smaller current will be applied to the area to be welded to pre-heat it. The three levels will be 1: no pre-heat, 2: moderate pre-heat, and 3: high pre-heat. The current used to achieve levels 2 and 3 will be selected by the welding operator at EWI based on past experience welding 304 SS tubes.

- Post-heat. After the welding passes, a smaller electrical current will be applied to the weld zone to heat it and possibly anneal the hard heat affected zone. Similar to the pre-heat, the three levels will be chosen by the operator and will be 1: no post-heating, 2: moderate post-heating, and 3: high post-heating.

Treatment group	Ni union width	Ni union diameter	Pre-heat	Post-heat
1	Thin	Small	None	None
2	Thin	Med.	Med.	Med.
3	Thin	Large	High	High
4	Med.	Small	Med.	High
5	Med.	Med.	High	None
6	Med.	Large	None	Med.
7	Thick	Small	High	Med.
8	Thick	Med.	None	High
9	Thick	Large	Med.	None

Table 3.7: Test matrix for future TIG welded specimens.

The other welding parameters such as current level, speed of travel and electrode geometry will be chosen by the orbital TIG welder operator based on past experience welding 304 SS tubes, as they were with the previous specimens.

The main effects of the four variables will be tested with a Taguchi L9 orthogonal array, so only nine treatment groups will be required. Several replications will be made within each treatment group so that the ultimate strength and fatigue properties of several specimens can be found. The test matrix is shown in Table 3.7.

After welding, the unmelted parts of the Ni union will be machined away before strength testing to clear up any uncertainty about whether it transmits stress. This has already been done on the welds in the demonstration actuator to be able to fit cartridge heaters inside the NiTi tube.

3.4 Adhesive Bonding

The last joining method presented here is adhesive bonding. Adhesives have the advantage of being a low temperature process and being able to bond to a wide variety of materials. The experience of the collaborators at Boeing with bonding titanium alloys helped to design the joints, choose the adhesives to be tested, and perform the proper surface preparation.

3.4.1 Specimen Design - Round 1

The first round of adhesive specimens were similar to the ultrasonically soldered (USS) specimens. Tube-and-socket joints were used so that the contacting area could be increased indefinitely. NiTi tubes were adhered to aluminum 2024 (Al 2024) blocks because this aluminum alloy is already widely used on aircraft for its high strength, low weight, and fatigue resistance. The similarities between the geometry and materials of the USS and adhesive specimens also aided comparison between the two methods.

Aluminum blocks that were 1" (25.4 mm) cubes were used as the grips on the first set of specimens. These blocks had a hole in the center of one of their faces which was 0.395" (10.0 mm) in diameter drilled to a depth called the "bond length," then 0.5" (12.7 mm) in diameter for the rest of the way through. The adhesive was only put on the 0.395" diameter part of the hole. The NiTi tubes had a 0.375" (9.5 mm) outer diameter and a 0.225" (5.72 mm) inner diameter, like the USS and TIG welded NiTi tubes. They were cut to be 1" (25.4 mm) longer than the bond depth. Two different bond depths were investigated: 0.25" and 0.5" (6.35 and 12.7 mm).

Two different adhesives were used. The first was Hysol EA 9394 which is a paste, and the second was Hysol EA 9696 OST Grade 10 which is a film. The aluminum grips had to be adjusted from the USS design to accommodate the EA 9696 film adhesive. It would not have been possible to apply an adhesive film between the outside of the NiTi tube and inside of the hole in the grip and apply pressure to it as is required for proper curing. So, the grips were cut in half, the film applied to each half, then the two pieces were clamped together for curing. This was also done on one set of EA 9494 paste adhesive specimens to see if this change in the grip design affected the strength. A drawing of the two different grips is shown in Figure 3.20 and a photograph of completed specimens is shown in Figure 3.21.

The bonds were assembled by Tyler Zimmerman of The Boeing Company. He removed the native oxide from the nitinol surface by abrasive blasting it with aluminum oxide grit followed by a thorough acetone solvent wipe to remove any debris. He ran water over the fresh surface to make sure it was water-break free. Then he sprayed or brushed applied a sol-gel product called AC-130, which needed to be done within a few hours to avoid re-oxidizing the surface. Once that was dry, he spray applied a corrosion inhibiting bond primer (BR 6747-1) that helped the adhesive wet the surface. This was then heat cured, then the adhesive was applied to the parts and they were assembled. C-clamps were used to clamps the aluminum grips together as the adhesives cured.

3.4.2 Ultimate Failure Tests - Round 1

The first round of testing's purpose was to investigate the effect of different adhesives, grip designs, bond depths, and test temperatures on the ultimate failure torque

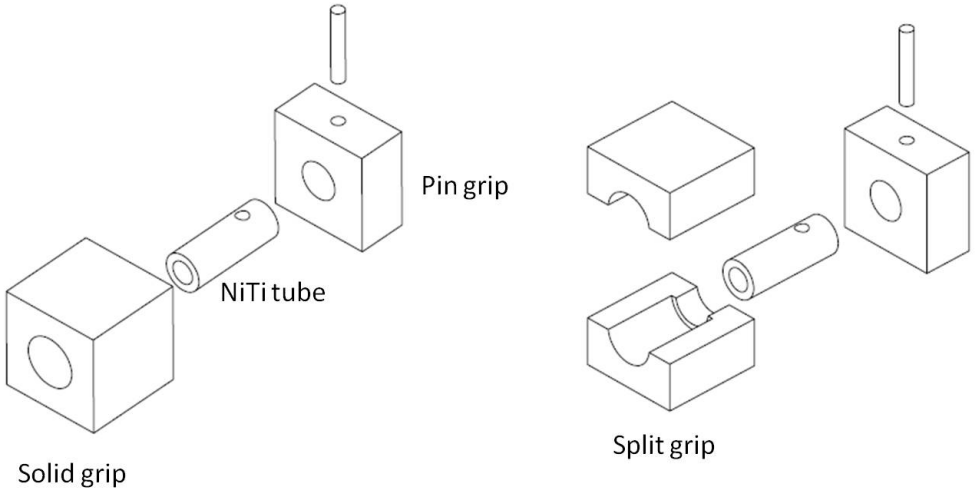

Figure 3.20: Split and solid aluminum grips for adhesive specimens.

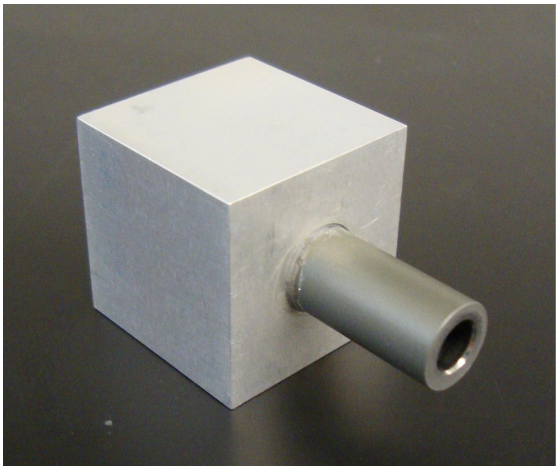

(a) EA 9394 adhesive specimen.

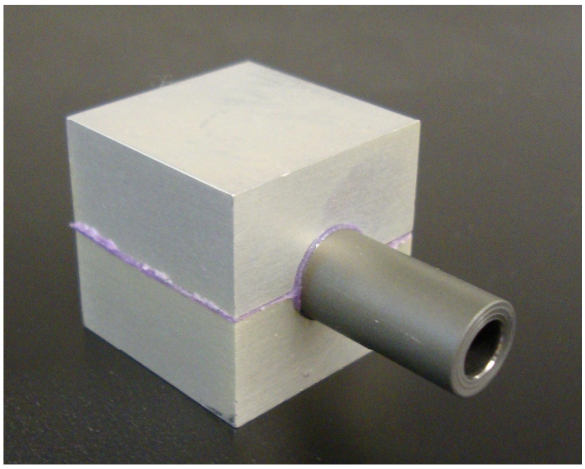

(b) EA 9696 adhesive specimen.

Figure 3.21: Assembled adhesive specimens.

Test Number	Adhesive	Test Temp. (°C) [°F]	Grip Type	Bond Depth (in) [mm]	Anticipated Failure Torque (in-lb) [N-m]	Number of Specs. Tested
1	EA 9696 Film	22 [72]	Split	0.25 [6.35]	350 [39.6]	3
2		82 [180]			250 [28.3]	3
3		121 [250]			120 [13.6]	3
4				0.50 [12.7]	240 [27.1]	1
5	EA 9394 Paste	22 [72]		0.25 [6.35]	230 [26.0]	3
6			Solid		230 [26.0]	3
7		82 [180]			165 [18.6]	3
8		121 [250]			130 [14.7]	3
9				0.50 [12.7]	260 [29.4]	3
10		22 [72]			460 [52.0]	2

Table 3.8: Adhesive test matrix.

of the joints. There were two different adhesives, two grip designs, two bond depths, and three test temperatures: room temperature, 82°C (180°F), and 121°C (250°F). Twenty-nine specimens were made and randomly assigned to different testing groups, which are described in the test matrix in Table 3.8. The anticipated failure torque was calculated based on lap shear data from tests that Boeing performed prior to this study.

All of the strength data collected is given in Appendix A. The average failure torque of the specimens in each treatment group is shown in Table 3.9. Two of the specimens failed at the pin holes in the NiTi tube instead of in the adhesive joint, so their data was ommitted. This was due to poorly drilled pin holes, a problem which was fixed for specimens tested after them.

Test Number	Adhesive	Test Temperature (°C) [°F]	Grip Type	Bond Depth (in) [mm]	Mean Failure Torque (in-lb) [N-m]	Standard Deviation (in-lb) [N-m]
1	EA 9696 Film	22 [72]	Split	0.25 [6.35]	349.7 [39.52]	22.5 [2.54]
2		82 [180]			252.5 [28.53]	39.8 [4.50]
3		121 [250]			165.7 [18.72]	16.4 [1.85]
4				0.50 [12.7]	93.5 [10.57]	N/A
5	EA 9394 Paste	22 [72]		0.25 [6.35]	315.2 [35.62]	43.0 [4.86]
6			Solid		328.4 [37.12]	46.1 [5.21]
7		82 [180]			145.5 [16.44]	20.1 [2.27]
8		121 [250]			108.3 [12.24]	21.1 [2.38]
9				0.50 [12.7]	198.5 [22.43]	20.3 [2.29]
10		22 [72]			415.2 [46.92]	24.7 [2.79]

Table 3.9: Measured adhesive test data.

The mechanical behavior of a specimen in test number 1 is shown in Figure 3.22. Both the deflection of the torsional machine's specimen grips and of the rotary extensometer mounted directly to the specimen are plotted. They both show the same basic behavior, but different stiffnesses because the extensometer's measurement region is smaller. It can be seen that detwinning in the NiTi tube takes place between about 170 and 200 in-lb (19 and 23 N-m), and that the detwinning is completed by the time that the specimen breaks at 361 in-lb (40.8 N-m).

The different types of grips (split and solid) and adhesives can be seen not to affect the mechanical behavior of the specimens in Figure 3.23. Both grips and both adhesives produce joints with very similar stiffnesses, though different strengths. The same thing can be seen with the different bond depths in Figure 3.24. Although the 0.5" bond depth is stronger than the 0.25" one, it is not stiffer nor does it have different detwinning torques or behavior.

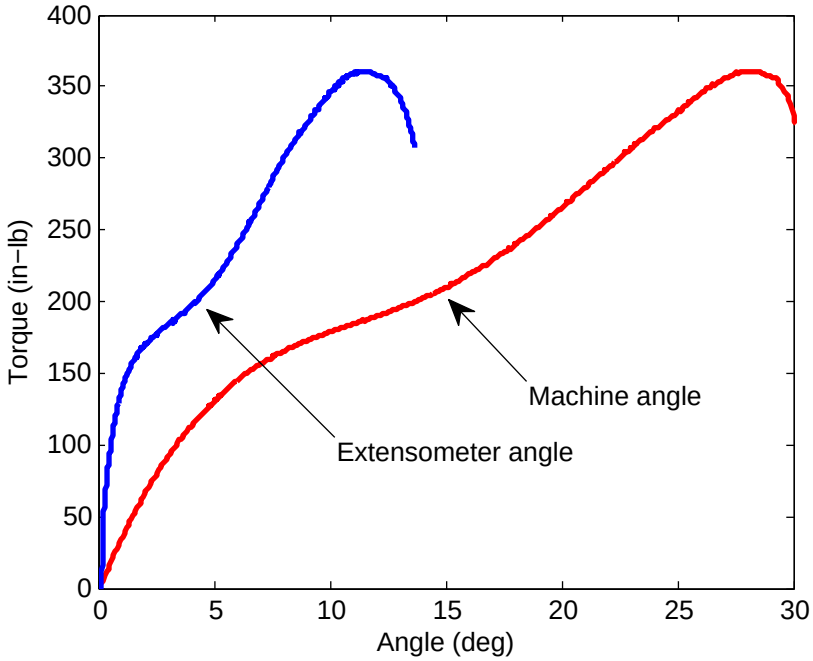

Figure 3.22: Mechanical behavior of adhesive specimen in test #1.

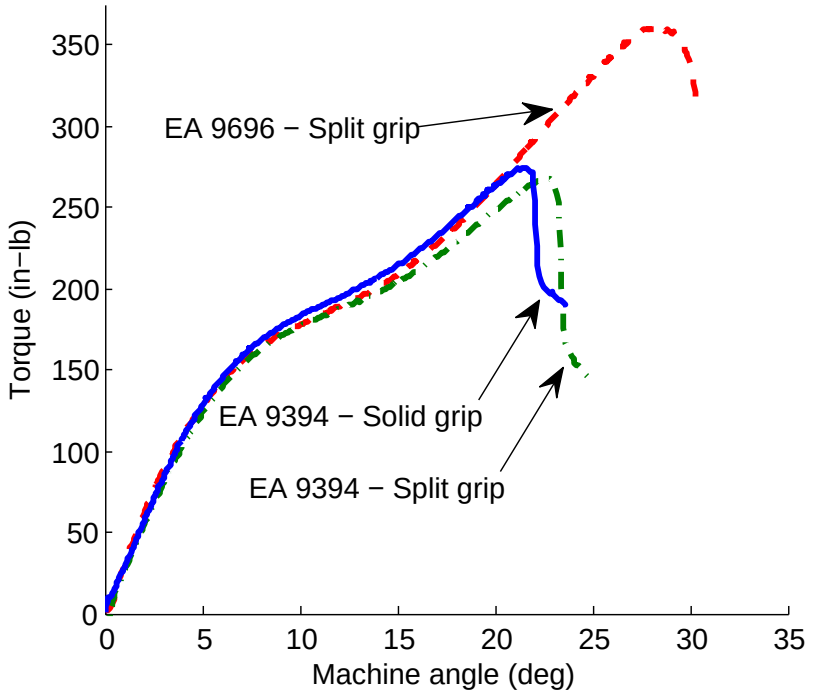

Figure 3.23: Mechanical behavior of different adhesives and grips.

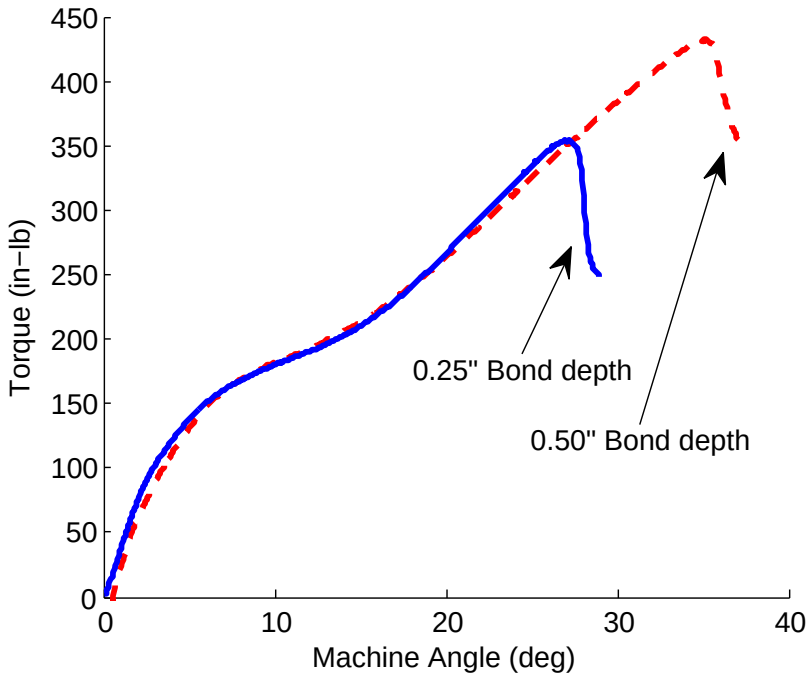

Figure 3.24: Mechanical behavior of different bond depths.

The testing temperature had a noticeable difference on the behavior of the specimens. At room temperature the NiTi tubes are in their shape-memory state, while at 121°C (250°F) they are superelastic. This difference in torque versus angle behavior can be seen in Figure 3.25

Statistical Analysis of Effect of Specimen Quality

Not all of the twenty-nine specimens used in this trial were of the same quality. Some of them were observed to have small gaps in their bond line or misalignment between the tubes and aluminum grips. When the specimens were being assigned to different testing groups it was ensured that each group had "good", "OK", and "bad" quality specimens.

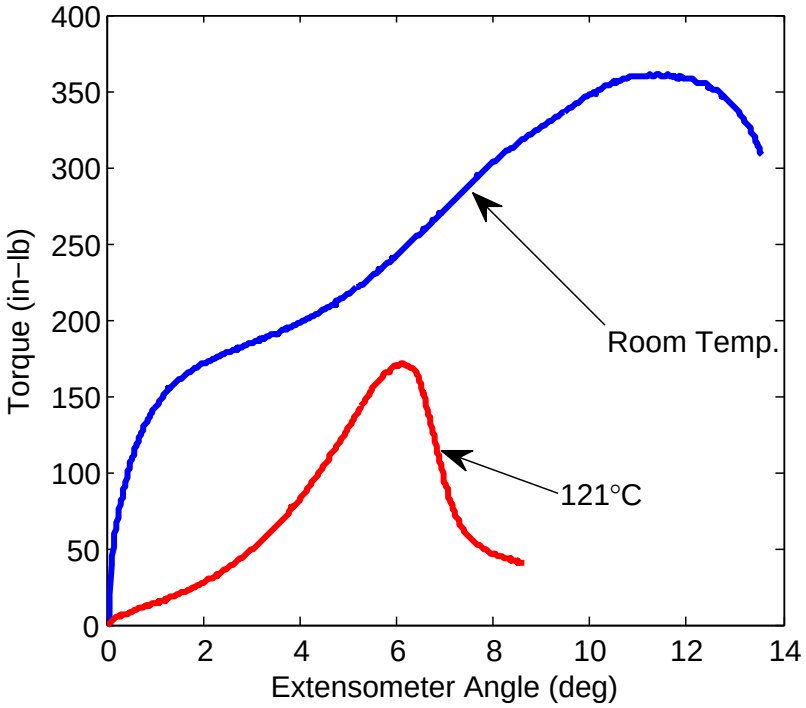

Figure 3.25: Mechanical behavior of adhesive specimens at different temperatures.

The data from the solid grips was examined to test if the specimens' quality affected their strength (the split grip data was not used for this because it had another possible factor affecting strength, which is discussed later). The statistical model used for this analysis was

$$T_{ijk} = \mu + \alpha_i + \beta_j + \epsilon_{ijk} \tag{3.7}$$

where T_{ijk} is the measured breaking torque of sample k in the group being considered, μ is the overall mean, α_i is the effect of test number i, β_j is the effect of quality j, and ϵ_{ijk} is the error term which is assumed to be independently, identically distributed with a zero mean and a constant normal variance. There were not enough specimens tested to evaluate whether there was any interaction between the quality and test number, so the main effects of each were all that could be solved for. The program Minitab was used to calculate an Analysis of Variance (ANOVA) table and a main effects plot, which are shown in Table 3.10 and Figure 3.26.

The P-value of the quality main effect was calculated to be 0.322, which is larger than the threshold of 0.05 to know that there was a statistically significant effect. The differences between the means of the three quality groups in Figure 3.26 are also small compared with the differences between the means of the test numbers. The main effect follows what one would expect it to be; the good specimens are the strongest, the bad are the weakest, and the OK ones are in between. Based on these factors, it was concluded that the quality probably had an effect, but it was small compared to the random variation. The small difference between the means of the quality groups probably was not due to random variation, but there was a physical cause for it. The magnitude of this physical effect was found and subtracted from the

Factor	Type	Levels	Values
Test Number	Fixed	5	6, 7, 8, 9, 10
Quality	Fixed	3	Good, OK, Bad

Source	DOF	Seq SS	Adj SS	Adj MS	F	P
Test Number	4	166306	142452	35613	46.65	< 0.001
Quality	2	2045	2045	1023	1.34	0.322
Error	7	5344	5344	763		
Total	13	173695				

S = 27.63 R-Sq = 96.92% R-Sq(adj) = 94.29%

Table 3.10: ANOVA table for effect of quality on adhesive strength data.

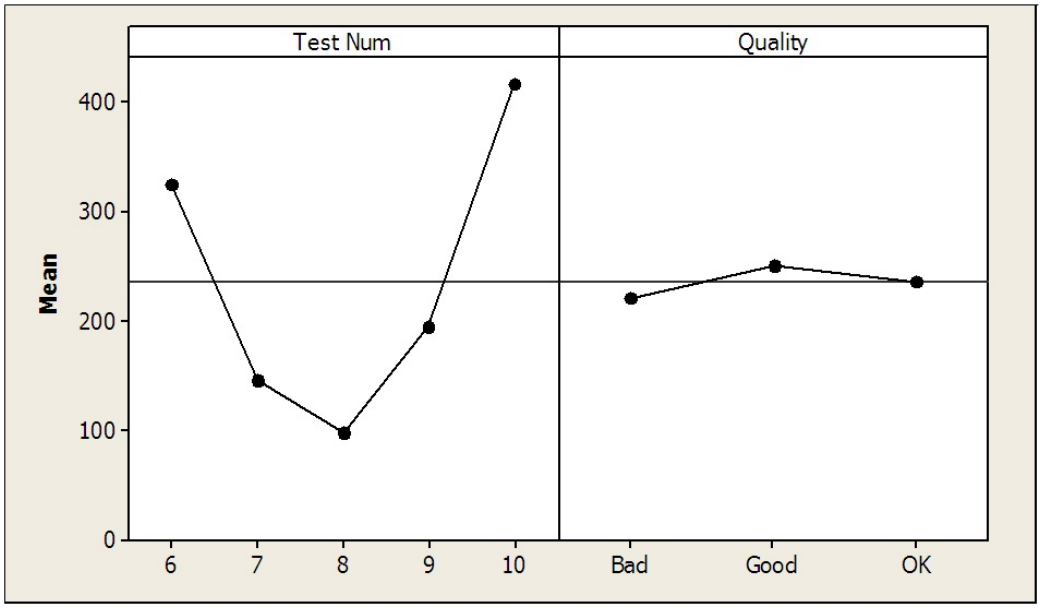

Figure 3.26: Main effect of quality on adhesive specimens' breaking torques.

Quality Group	Mean (in-lb)	Main Effect (in-lb)
Good	249.6	+13.4
OK	236.2	0
Bad	220.9	-15.3

Table 3.11: Calculated effect of quality on breaking torque.

measurements to come up with an approximation of what the failure torque would have been if all the specimens were the same quality. This magnitude is shown in Table 3.11

In subsequent analysis the measured failure torque for the good specimens has 13.4 in-lb (1.51 N-m)subtracted from it, the OK specimens' is left unchanged, and the bad specimens has 15.3 in-lb (1.73 N-m) added to it. This approximates what the failure torque would have been if all of the specimens were of medium quality.

Statistical Analysis of Clamping Force

Another factor that could have possibly affected the breaking torque of the split grip specimens was the force with which they were clamped into the torsional machine. The square aluminum blocks adhered to the NiTi tubes were clamped between two V-grooves which were attached to the torsional machine. The force that the V-grooves were clamped together could have put extra pressure on the bond line, affecting its strength. This was investigated by varying the amount of clamping force between "tight" which was as tight as the clamping screws could be made, and "loose" which was just tight enough to hold the aluminum grips in the V-grooves. The statistical model used to analyze the effect was the same as for the specimen quality, (3.7), except that β_j was the main effect of the clamping force, not quality. The ANOVA

Factor	Type	Levels	Values
Test Number	Fixed	5	1, 2, 3, 4, 5
Clamp Force	Fixed	2	Loose, Tight

Source	DOF	Seq SS	Adj SS	Adj MS	F	P
Test Number	4	86651	83770	20943	26.89	< 0.001
Clamp Force	1	228	228	228	0.29	0.606
Error	7	5451	5451	779		
Total	12	92330				

S = 27.91 R-Sq = 94.10% R-Sq(adj) = 89.88%

Table 3.12: ANOVA table for effect of clamping force on adhesive strength data.

Clamping Force	Main Effect (in-lb)
Loose	+5.34
Tight	-5.34

Table 3.13: Calculated effect of clamping force on breaking torque.

Table from this analysis is shown in Table 3.12, and a plot of the calculated main effects is shown in Figure 3.27.

The calculated P-value for the clamping force was 0.606 in Table 3.12 and the difference between the means, seen in Figure 3.27, was small, so it was concluded that the clamping force probably did not have a large effect. The calculated effect of the clamping force is shown in Table 3.13. The difference is only ± 5.3 in-lb (0.6 N-m), so if this adjustments made by subtracting the effect shown in Table 3.13 are wrong, they do not affect the conclusions described later.

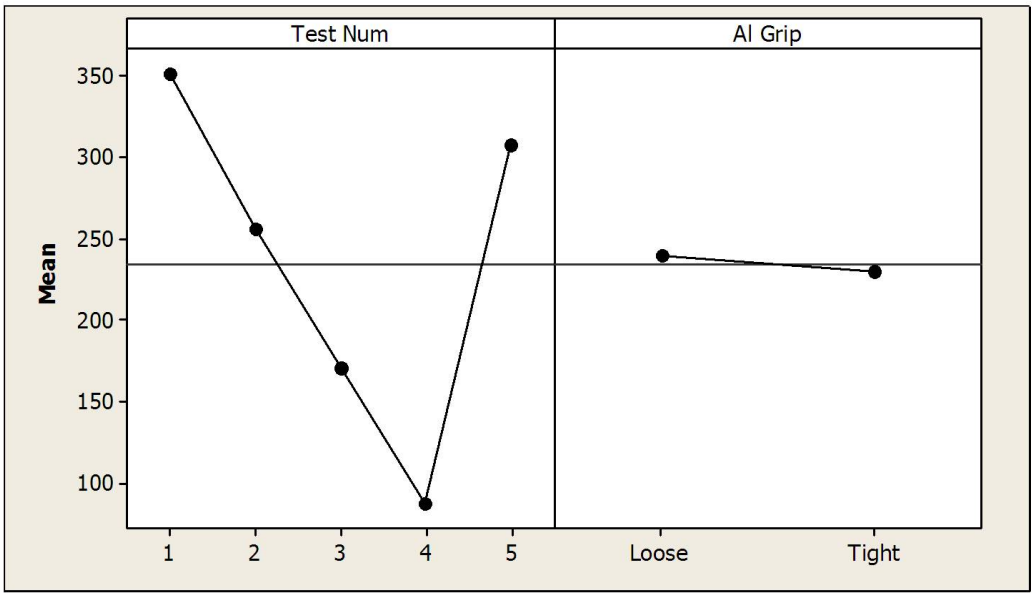

Figure 3.27: Main effect of clamping force on adhesive specimens' breaking torques.

Statistical Analysis of NiTi Tube Misalignment

The last factor that was investigated to see if it affected the specimens' breaking torques was the misalignment between the NiTi tubes and aluminum blocks. The first few specimens made had up to a 2° misalignment in them. The alignment for every specimen was measured photographically, then analyzed as a covariate with the only main effect being the test number. The statistical model for this was

$$T_{ij} = \mu + \alpha_i + \beta_{ij} + \epsilon_{ij} \tag{3.8}$$

Factor	Type	Levels	Values
Test Number	Fixed	10	1, 2, 3, 4, 5, 6, 7, 8, 9, 10

Source	DOF	Seq SS	Adj SS	Adj MS	F	P
Misalignment	1	18	489	489	0.75	0.398
Test Number	9	264918	264918	29435	45.41	< 0.001
Error	16	10372	10372	648		
Total	26	275308				

S = 25.46 R-Sq = 96.23% R-Sq(adj) = 93.88%

Table 3.14: ANOVA table for effect of misalignment on adhesive strength data.

where μ is the overall mean again, α_i is the main effect of test number i, and β_{ij} is the effect of the misalignment. The ANOVA Table for the analysis of the covariate model is shown in Table 3.14.

The calculated P-value for the misalignment covariate was 0.398, which is high enough that it can be concluded that it likely did not affect the strength of the specimens.

Adjusted Strength Data

Based on these analyses of factors that could possibly affect the breaking torque of the adhesive specimens, the measured breaking torque was adjusted for the specimen quality and clamping force by subtracting out their calculated effects, while the effect of misalignment was not subtracted out. The means and standard deviations of the adjusted test data for each testing group are shown in Table 3.15, and the shear strengths, calculated with (3.4), are in Table 3.16.

Test Number	Adhesive	Test Temperature (°C) [°F]	Grip Type	Bond Depth (in) [mm]	Mean Failure Torque (in-lb) [N-m]	Standard Deviation (in-lb) [N-m]
1	EA 9696 Film	22 [72]	Split	0.25 [6.35]	351.2 [39.69]	10.5 [1.19]
2		82 [180]			255.6 [28.88]	37.6 [4.25]
3		121 [250]			171.0 [19.32]	16.4 [1.85]
4				0.50 [12.7]	88.2 [9.97]	N/A
5	EA 9394 Paste	22 [72]		0.25 [6.35]	308.0 [34.80]	31.1 [3.51]
6			Solid		324.6 [36.68]	29.5 [3.33]
7		82 [180]			146.1 [16.51]	12.5 [1.41]
8		121 [250]			99.4 [11.23]	14.0 [1.58]
9				0.50 [12.7]	194.7 [22.00]	20.8 [2.35]
10		22 [72]			416.2 [47.03]	45.0 [5.08]

Table 3.15: Adjusted adhesive test data.

Test Number	Adhesive	Test Temperature (°C) [°F]	Grip Type	Bond Depth (in) [mm]	Mean Shear Strength (ksi) [MPa]	Standard Deviation (ksi) [MPa]
1	EA 9696 Film	22 [72]	Split	0.25 [6.35]	6.03 [41.6]	0.18 [1.2]
2		82 [180]			4.39 [30.3]	0.65 [4.5]
3		121 [250]			2.93 [20.3]	0.28 [2.0]
4				0.50 [12.7]	0.757 [5.22]	N/A
5	EA 9394 Paste	22 [72]		0.25 [6.35]	5.29 [36.5]	0.53 [3.7]
6			Solid		5.58 [38.5]	0.51 [3.5]
7		82 [180]			2.51 [17.3]	0.21 [1.5]
8		121 [250]			1.71 [11.8]	0.24 [1.66]
9				0.50 [12.7]	1.67 [11.5]	0.18 [1.2]
10		22 [72]			3.58 [24.7]	0.39 [2.7]

Table 3.16: Calculated adhesive shear strengths.

Test number 4 should be considered an outlier and should not be taken into consideration when making judgments about the effect of the test variables. There was only one specimen in that treatment group, so it cannot be ascertained for certain whether its unusually low strength was the result of the test variables or defects in its manufacturing. However, when it was disassembled the adhesive looked qualitatively different than all of the other specimens. It is suspected that too much clamping pressure was applied to this specimen during curing, which squeezed out the adhesive resin from the nylon carrier, and did not leave much adhesive in the bond. A more consistent clamping pressure in the construction of the next specimens will fix this problem.

By comparing Tables 3.9 and 3.15 it can be seen that the adjustments affected the standard deviations in each test group more than the means. The largest change in mean was in test number 8 (EA 9394 adhesive, 121° C, solid grip, 0.25" bond depth) which decreased by 8.9 in-lb (1 N-m), or about 8%. On average, the adjustments only changed the mean of each test group by 1.6 in-lb (0.18 N-m), which was a change of only 0.7%. However, the effect on the standard deviations was more noticable. On average, the standard deviation within each test group dropped by 4 in-lb (0.5 N-m), which was a change of 16%. This means that a lot of the variation observed within the test groups was the result of different specimen qualities and clamping forces.

Analysis of Test Variables

Now that the data was adjusted for effects that were not intended to affect the specimens' strengths, the effect of the test variables was investigated. Two different ANOVA Tables were constructed. The first looked at the main effect of each test variable: grip type, adhesive type, overlap and temperature. This analysis did not

Factor	Type	Levels	Values
Grip Type	Fixed	2	Solid, Split
Adhesive	Fixed	2	EA 9696, EA 9394
Overlap	Fixed	2	0.25", 0.50"
Temperature	Fixed	3	21°C, 82°C, 121°C

Source	DOF	Seq SS	Adj SS	Adj MS	F	P
Misalignment	1	370	752	752	0.82	0.376
Grip Type	1	16775	7	7	0.01	0.929
Adhesive	1	5161	9874	9874	10.81	0.004
Overlap	1	27452	30544	30544	33.44	< 0.001
Temperature	2	184342	184342	92171	100.92	< 0.001
Error	19	17353	17353	913		
Total	25	251454				

S = 30.22 R-Sq = 93.10% R-Sq(adj) = 90.92%

Table 3.17: ANOVA table for effect of all test variables on adhesive strength data.

have enough degrees of freedom left over to investigate interaction effects. The second analysis only looked at adhesive and temperature, but did analyze the interaction between them.

The ANOVA Table calculated for all of the main effects, still with misalignment as a covariate is shown in Table 3.17, and a plot of all of the main effects is shown in Figure 3.28.

The ANOVA Table for the interaction between the temperature and adhesive type is shown in Table 3.18, and a plot is shown in Figure 3.29. The calculated P-value for the interaction was 0.011, so there is a statistically significant interaction, but by examining the plot, it can be seen that the two curves are nearly parallel. This means that although there is some interaction (enough for the ANOVA to pick up), it

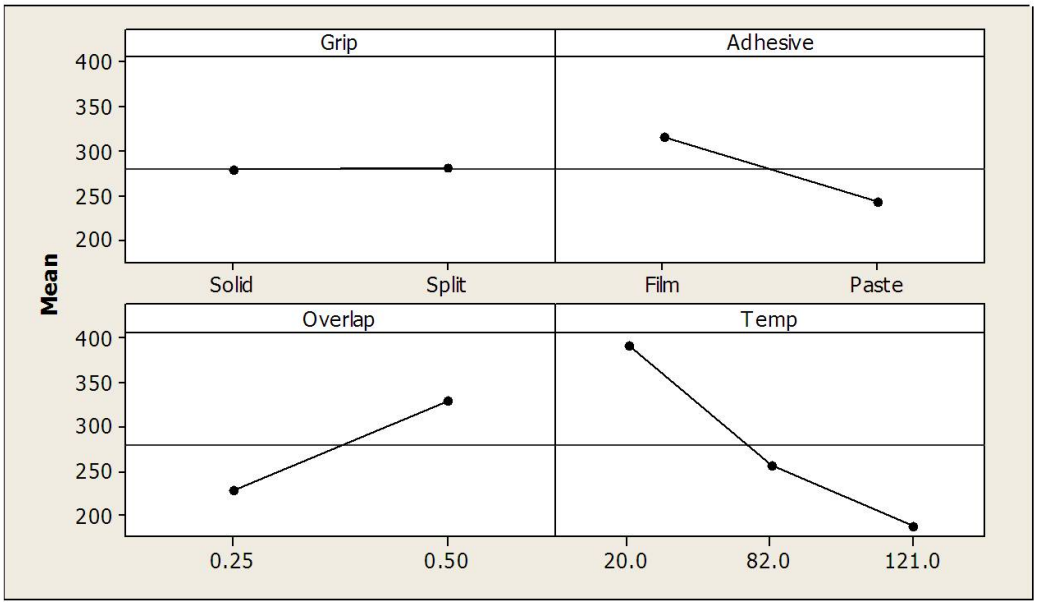

Figure 3.28: Main effects of all test variables on adhesive specimens' breaking torques.

is likely not large enough to be of practical concern. Both adhesives get weaker with increasing temperatures at about the same rate, and the EA 9696 is always stronger than the EA 9394.

3.4.3 Specimen Redesign - Round 2

Based on the results of the first round of tests, changes were made to the specimen design for the second round. This round includes elevated temperature creep tests and thermomechanical cycling tests in addition to ultimate strength tests. Only the stronger EA 9696 adhesive was used, which requires the split aluminum grips, and as much unnecessary material as possible was eliminated from the aluminum grips. This speeds up the thermal cycling of the specimens. The back 0.5" (12.7 mm) or

Factor	Type	Levels	Values
Adhesive	Fixed	2	EA 9696, EA 9394
Temperature	Fixed	3	21°C, 82°C, 121°C

Source	DOF	Seq SS	Adj SS	Adj MS	F	P
Misalignment	1	547	1866	1866	4.20	0.060
Adhesive	1	7620	27953	27953	62.90	< 0.001
Temperature	2	160933	142990	71495	160.88	< 0.001
Adhesive × Temperature	2	5574	5574	2787	6.27	0.011
Error	14	6222	6222	444		
Total	20	180895				

S = 21.08 R-Sq = 96.56% R-Sq(adj) = 95.09%

Table 3.18: ANOVA table for interaction of temperature and adhesive effects on adhesive strength data.

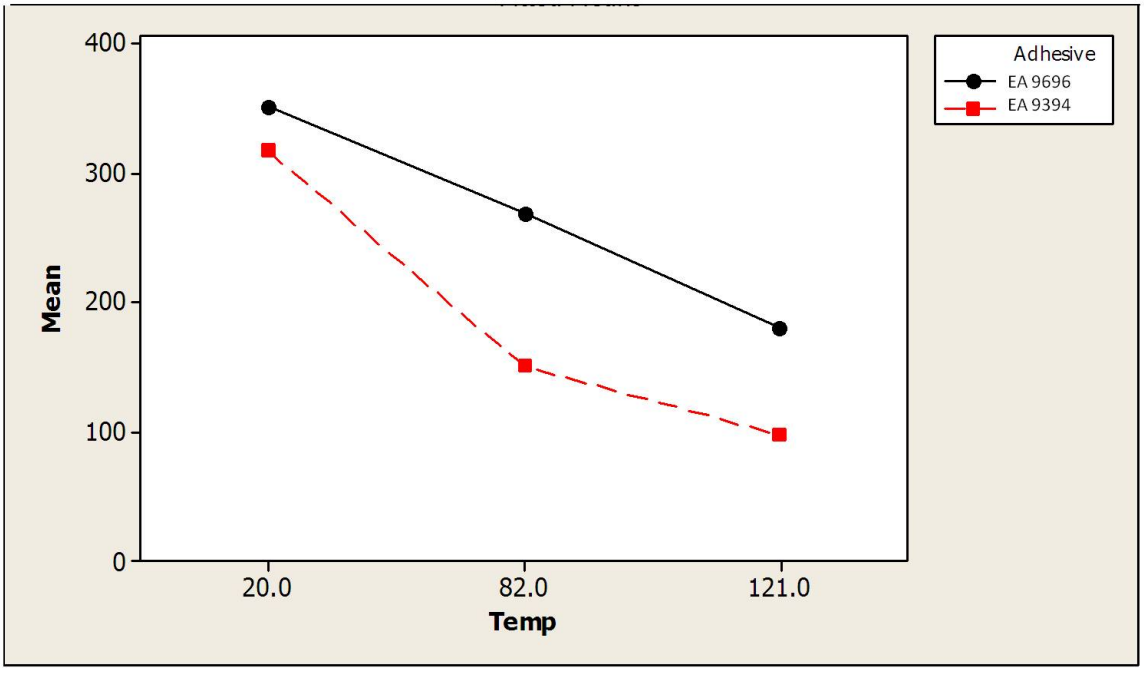

Figure 3.29: Interaction of adhesive and temperature.

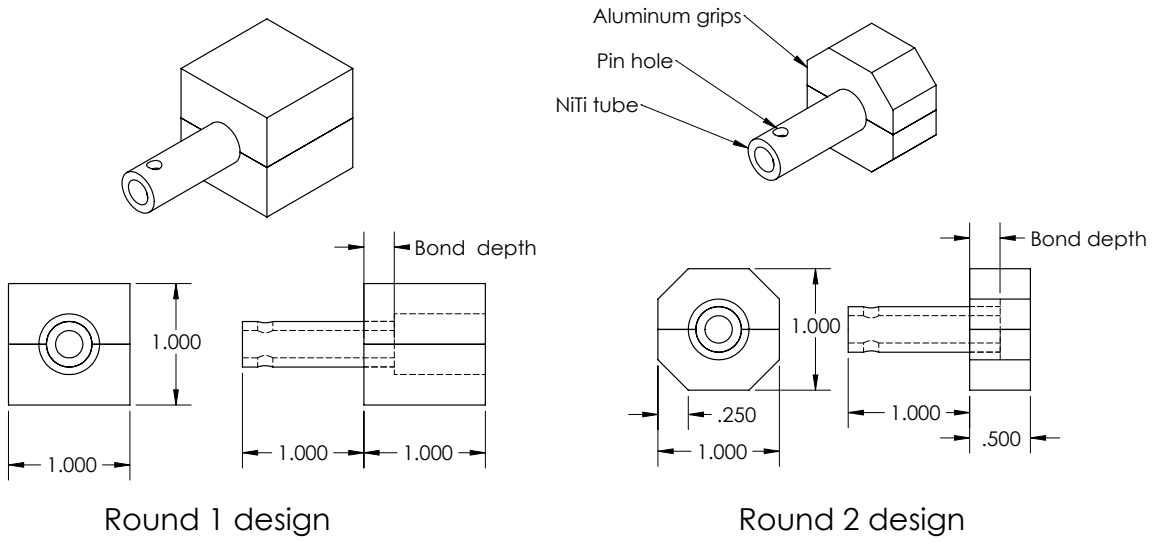

Figure 3.30: Changes made to adhesive grips.

the aluminum grips was removed and chamfers were out of the corners of the blocks after assembly. These changes are shown in Figure 3.30.

3.4.4 Future Work

Ultimate Failure Tests - Round 2

The next task for this adhesives joining project is to conduct several ultimate failure tests on round 2 specimens. These will be performed the same way that the round 1 tests were, and will help design the following creep and cycling tests. These tests will ensure that the specimen changes, and modifications made to the testing machine in between the two rounds do not affect the measured strength of the specimens.

Creep Tests

High temperature, constant torque creep tests will be done after the ultimate failure tests. These will be run at a constant torque of 50% and 75% of the failure torque at the test temperature, found in the ultimate failure tests. Room temperature and 121°C (250°F) will be the test temperatures. These will be run for 24 hours on each specimen to measure the time-based deflection of the bonds under a constant stress.

Thermal Cycling Tests

Thermomechanical cycling tests will also be conducted to simulate the use of these adhesive joints in an actuator. The specimens can be subjected to either a constant, "dead" load or a load that varies with temperature to simulate actuating against a spring load. The NiTi in these specimens will not have a two-way shape memory effect trained into it, so simply actuating against a spring is not possible, so the torque applied to the tube will be varied as a function of the temperature to simulate this. The temperature will be cycled between near room temperature, 25°C (77°F) to 121°C (250°F) and back by the heaters and vortex tubes. One of these cycles can be completed in just under 10 minutes, so roughly 150 cycles can be completed in 24 hours, and 1000 cycles per week.

These tests will be run with torques determined from the ultimate failure tests. The number of cycles that these tests will be run for is not currently known.

Chapter 4: CONCLUDING REMARKS: EVALUATION OF JOINING METHODS

This last chapter compares the joining methods described in detail in Chapter 3. A table summarizing the main advantages, disadvantages, test results and applications of each method is shown in Table 4.1. That information is expanded upon in the following sections.

4.1 Ultrasonic Soldering

Ultrasonic soldering (USS) is a lead-free, fluxless soldering process where neither base metal is melted, only the solder in between them is melted.

4.1.1 Advantages

USS takes place at 250°C (480°F), which does not affect the previous training a NiTi workpiece may have undergone. No heat affected zone (HAZ) is formed, which is where many welded joints are weakest and fail.

Because large surfaces can be soldered together, the joint strength can be increased by increasing the bonding area. The bond depth of the tube-and-socket joints manufactured in this study can be increased to increase the breaking torque of the joints.

Method	Advantages	Disadvantages	Applicable Materials	Joint Geometry	Shear Strength (ksi) [MPa]	Other Results	Projection
TIG welding	Readily available, inexpensive equipment. Applicable to wide variety of metals. Capable of deeper penetration welds than laser welding.	Larger effect on Shape Memory Effect (SME) than laser welding	Most metals	Butt welds between NiTi and 304 SS tubes	50 [350]	Penetration of 0.040" (1 mm) in single pass. HAZ 125μm wide.	Most useful for joining large NiTi pieces to metallic machinable structures when strength is important. Optimal application are where partial loss of SME in the HAZ can be easily compensated for by adding more NiTi.
Laser Welding	Smaller HAZ and effect on SME than TIG welding. Applicable to wide variety of metals	Shallower weld penetration than TIG, requires more weld passes. Expensive equipment.	Most metals	Thin wall: Butt welds between NiTi and 304 SS tubes.	Thin wall: 60 [410]	Thin wall max single-pass penetration 0.020" (0.5 mm). HAZ 8μm wide.	Most applicable for smaller NiTi components with highest strength requirements. Such components will likely have weld penetrations of less than 1/8" but will benefit from the minimal loss of the SME due to a very narrow HAZ.
				Thick wall: Bevel welds between NiTi to 304 SS tubes	Thick wall: 50 [350]	Thick wall multi-pass penetration 0.065" (1.65 mm). HAZ 20μm wide	
Ultrasonic Soldering (USS)	Low temperature process, so no HAZ and little effect on SME. Does not require fluxes or Pb-based solder. Joint design easily modified to increase strength. Applicable to many metals and non-metals.	Solder has relatively low melting point so it may become weak near NiTi operational temperatures	Non-ferrous metals, ceramics, glass	Tube and socket joints between NiTi tubes and Al 2024 blocks	5.3 [37]	No HAZ or loss of SME	Applicable for components that will not be subjected to high temperatures. Strength requirements are flexible by varying the joint area. USS is optimal for lap-shear joints and may be useful for bimorph applications such as bimetallic beams.
Adhesive Bonding	Low temperature process like USS. Joint design easily modified to increase strength. Applicable to many materials.	Joints become weaker with higher temperatures. Requires chemicals which have safety and disposal precautions.	Most metals and non-metals	Tube and socket joints between NiTi tubes and Al 2024 blocks	Room temp: 6.0 [42] At 121°C: 2.9 [20]	No HAZ or loss of SME	Similar applications as USS. Joints should be designed in a lap-shear configuration. Depending upon the adhesive used, adhesive joints may be able to withstand higher environmental temperatures than USS joints.
Machining	Low temperature process (if adequate coolant used). Strong (if splines are used), simple (if pins or clamps are used).	Difficult and expensive. Pins and clamps weaker than other joining processes.	Any materials	Splines, friction clamps, pin holes	N/A	Splines have performed well for training NiTi tubes. Clamps slip at high torques. Material at pin holes detwins/yields rest of tube.	Splines good for high-strength applications where proven technology is needed and high cost is acceptable. Clamps and pin holes applicable where less stiffness is acceptable.

Table 4.1: Comparison of joining methods.

Many materials can be soldered together. The USS process is able to solder difficult to wet materials such as aluminum and titanium alloys, ceramics and glass. The tough oxide layer than builds up on the surface of aluminum and titanium alloys which prevents normal solder from forming strong joints with them is broken up by the ultrasonics.

Although USS equipment is more expensive than regular soldering equipment, it is not as expensive as orbital TIG or laser welding equipment. This is especially important if fewer joints need to be made, when high upfront cost of machinery cannot be spread out over many parts.

4.1.2 Disadvantages

USS produces joints with a weaker shear strength than fusion welding methods. The contacting area can be increased to produce joints with the same breaking torque, but this constrains more NiTi in the joint. Because the solder melts at 250°C and equi-atomic NiTi's austenite finish temperature can be as high as 100°C, these joints may be weaker at the high end of the operating temperature of a NiTi-based actuator. Creep may also be an issue, especially with constant loads at high temperatures. These concerns would have to be studied further before this process could be deemed suitable for an application.

4.1.3 Applications

The ideal applications for USS are for relatively low temperature operation, which could be done by using alloys of NiTi with austenite finish temperatures well below the weakening temperature of the solder. Geometries where large contacting surfaces can be joined would also be good for USS, such as bi-metallic beams where a trained

NiTi beam is joined to a non shape memory alloy beam that acts as a bias spring, or to another shape memory alloy beam that actuates in the opposite direction.

4.1.4 Joint Design

As stated previously, large contacting surface areas are crucial for producing strong USS joints, so tube-and-socket joints were used for this study. These could transmit enough torque to detwin the NiTi tubes in the joints. The joint geometry can be designed with (3.4), which gives

$$d \times r^2 = \frac{T}{2 \times \pi \times \tau} \tag{4.1}$$

where d is the bond depth, r is the radius of the tube, T is the torque on the joint, and τ is the shear strength. The average shear strength of the five specimens tested in Section 3.1.2 was 5.35 ksi (36.9 MPa), with a standard deviation of 0.33 ksi (2.3 MPa). These tests were conducted at room temperature, so the high-temperature strength of these joints is not yet known.

4.2 Laser Welding

Laser welding is a fusion welding process which uses a focused laser beam as a heat source. NiTi tubes were welded to 304 stainless steel tubes in this study, using a pure nickel interlayer to prevent hot cracking in the NiTi and the formation of brittle Ti-Fe intermetallics.

4.2.1 Advantages

Laser welding produced the strongest joints in this study. It also created a smaller heat affected zone than TIG welding. Although it is currently less commonly used

than TIG welding, it is already used some in the aerospace industry. Laser welding can also be used to join NiTi to a wide variety of metals, especially if proper interlayers are used.

4.2.2 Disadvantages

The laser heat source cannot make as deep penetration welds as TIG welding. The deepest penetration made in a single-pass has been about 0.020" (0.5 mm). Deeper welds can be made, as they were with the thick-walled bevel welds in Section 3.2.1, but these require more weld passes and were not as consistent as the single-pass welds.

Laser welding equipment is more expensive than TIG welding equipment, and there is less experience with it in industry.

4.2.3 Applications

Laser welding is best for applications where strength is critical. These will especially be small parts because of the shallower weld penetration. High up-front costs must be also acceptable. These factors make laser welding particularly suited for the aerospace and medical industry.

4.2.4 Joint Design

Joints between NiTi and 304 SS tubes strong enough to fully detwin the NiTi were made with butt and bevel welds. Laser welding could also be used to join NiTi wire to stainless steel attachments. Thin-walled tubes are not well suited for torque tubes because of their susceptibility to buckling, so for torsional actuators, thick-walled tubes with bevel welds would be best. Using (3.5), the radii of a tube can be designed for a given shear strength and torque by

$$\frac{r_o}{r_o^4 - r_i^4} = \frac{\pi \times \tau}{2 \times T} \tag{4.2}$$

where r_o and r_i are the outer and inner radii, respectively. The average shear strength, τ, of three thin-walled tubes tested in Section 3.2.2 was 66.3 ksi (457 MPa) with one outlier at 45.3 ksi (312 MPa). The thick-walled tube which was mechanically tested was weaker, with a shear strength of only 50.2 ksi (346 MPa).

The thin-walled tubes tested in Section 3.2.2 did not buckle only because of the added rigidity provided by the unmelted Ni union inside the tubes. No other tubes with those same wall thicknesses, without that insert, could be made to fail in shear before buckling. Even when there was only 0.25" (6.3 mm) of tube free between the grips and the tubes were steel they still buckled. NiTi is particularly prone to buckling because its martensite modulus of elasticity is less than half of aluminum's, and less than a sixth of steel's. And, when detwinning, the stiffness is even lower. However, no thick-walled NiTi tubes bucked in all of these tests, so it is recommended to use wall thicknesses at least as thick as those, which were 0.065 in (1.65 mm) thick.

4.3 TIG Welding

Tungsten inert gas (TIG) welding is another fusion welding process which uses an electric current from a non-consumable tungsten electrode to heat the workpieces while an inert shielding gas (usually argon) protects the weld from oxidation and atmospheric contamination.

4.3.1 Advantages

TIG welding produces strong joints, though not quite as strong as laser, but is much more common. TIG is already widely used in industry, particularly for fabricating and repairing aluminum, titanium and stainless steel parts. It can also provide much deeper weld penetration than laser welding, which makes it capable of welding thicker pieces, or making fewer welding passes. Like laser welding, NiTi could be joined to a variety of other metals as long as care is taken to select a proper interlayer.

4.3.2 Disadvantages

Although the TIG welded joints in this study were stronger than the yield strength of annealed 304 SS, they were not quite as strong as the laser welded joints. TIG welding also produces a larger heat affected zone than laser welding because it puts more heat into the workpieces. This degrades the shape memory effect more, requiring slightly more NiTi in an actuator to get the same capabilities.

4.3.3 Applications

TIG welding is best suited for thick joints where strength is important, but not quite as critical as for laser welding. The equipment for TIG welding is also less expensive than for laser welding, so the up-front costs will be lower. Because of the deeper weld penetration, TIG welding would probably be better than laser welding for joining thick-walled tubes in a torsional actuator.

4.3.4 Joint Design

TIG welded joints can be designed in the same way as laser welded joints, using (4.2). The two specimens which were strength tested had an average shear strength between 45 and 60 ksi (310 and 410 MPa). The uncertainty is due to the incomplete weld penetration through the tube walls, which is described in more detail in Section 3.3.3. Complete penetration welds on thick-walled tubes will have to be made to find the strength more accurately.

4.4 Adhesives

4.4.1 Advantages

Adhesives have many of the same advantages as USS. They are a low-temperature process, so the shape memory effect is undisturbed and no heat affected zone is created. The joint strength can also be increased by increasing the contacting area. They can be used to join NiTi to a wide variety of materials, and they are already widely used in the aerospace industry, so there is a lot of experience with them.

There is also little up front cost for adhesive bonding. An autoclave, the adhesive, and the surface preparation chemicals are all that is required.

4.4.2 Disadvantages

The strength of adhesive joints decreases with temperature. So, more care must be taken not to overheat these joints than with welded joints. Also, much more NiTi will be consumed in an equally strong joint with adhesives than with welding because much more contacting area will be needed to get a strong adhesive bond.

Temperature (°C) [°F]	Shear Strength (ksi) [MPa]	Standard Deviation (ksi) [MPa]
Room Temp	6.03 [41.6]	0.18 [1.2]
82 [180]	4.39 [30.3]	0.65 [4.5]
121 [250]	2.93 [20.3]	0.28 [2.0]

Table 4.2: Shear strength of EA 9696 adhesive at elevated temperatures.

The process of preparing the surfaces to be bonded and making the joints uses hazardous chemicals that must be handled and disposed of properly to be safe. This adds cost and complexity to the joining process.

4.4.3 Applications

Adhesives are well suited for joints where strength is not as critical as for welded joints, and where more NiTi can be used in the joint to get a large contacting area. The aerospace industry already uses many adhesives, so this is a promising process for integrating NiTi components into aircraft actuators and structures. Also, the low up-front cost and overhead makes adhesives ideal for prototyping and small production runs.

4.4.4 Joint Design

Adhesive joints should be designed in the same way as USS joints, with (4.1). The strength of the Hysol EA 9696 adhesive with a 0.25" (6.35 mm) bond depth at different temperatures is given in Table 4.2.

4.5 Machining

Although the purpose of this research is to avoid machining NiTi pieces, some of it had to be done to prepare and test NiTi specimens. The relative merits of machining NiTi for joints are discussed here, as well as which machining processes were found to be doable with NiTi tubes.

4.5.1 Advantages

Many parts are joined together via mechanical means already. This means that if NiTi pieces could be machined similarly, it could use existing designs which have already been tested and proven. Strong joints can be made by machining NiTi, and those pieces can then be joined to any other machinable material. As long as care is taken to use proper coolant, machining is a low temperature process, so many of the advantages of USS and adhesive apply, such as no loss of prior training or creating of a heat affected zone.

4.5.2 Disadvantages

NiTi is incredibly difficult to machine. It will often chatter horribly, it causes high tool wear, and machining processes often leave a poor surface finish (see Section 3.4.2 where two specimens failed due to this). Only a few operations can be done by cutting, most features must be ground or made by electro discharge machining (EDM), which are more expensive and time consuming.

4.5.3 Applications

The applications for mechanical joining of NiTi to structural materials vary by the method. Splines are used extensively by the Boeing Company for characterizing

NiTi tubes. The tubes used for the demonstration actuator in Section 3.3.5 initially had splines on their ends to train them before they were used in the demonstration actuator. The splines form strong joints, but take up a significant portion of the length of a NiTi tube, much the same way that a deep USS or adhesive joint would. So, they are suitable for long NiTi tubes.

Friction clamps and best suited for low-strength applications because they slipped at high torques. Their strength could not be increased indefinitely by making them longer because some of the NiTi tubes inside the grips started to slip while the rest of the material in the grip did not. These problems are described in Section 2.2.1. They are best suited for thinner-walled NiTi tubes where the detwinning torques are lower, but the tube still has a large radius from the axis of rotation to the surface where the grips apply friction. Tight-fitting rigid pins must be used inside the NiTi tube when it is clamped to prevent it from collapsing.

Pin holes are useful for applications where strength is more important than for the friction clamps, but stiffness is not. These were used to fixture the non-joined end of NiTi tubes to find the strength of most of the joints in this research. There is significant stress amplification at the pin holes (described in Section 2.2.2), so the material around the pins starts to detwin or yield at a much lower torque than the rest of the tube. The effect this has on fatigue is not yet known.

4.5.4 Tool Material

When cutting NiTi, new, sharp tools are essential. Because of this, high speed steel (HSS) tool bits are sometimes preferable to tungsten carbide because they can be re-sharpened much easier. Turning, facing, and grooving NiTi tube on a lathe

was found to be easiest with HSS bits that were sharpened immediately before being used, while drilling pin holes was found to be easiest with carbide drill bits. The carbide drill bits probably worked better than HSS ones because their added rigidity prevented chattering. Sharp bits reduce cutting forces and that along with a rigid setup reduces chattering.

NiTi can be ground and EDM cut just like any other material, so no special procedures are necessary for using those processes.

4.5.5 Cutting Tubes to Rough Length

NiTi tubes have been cut to length by two means: a cutoff tool on a lathe and an abrasive cutoff saw. When using a lathe, a low rotational speed is essential, and when using an abrasive saw, much coolant must be used.

4.5.6 Facing Tubes to Precise Length

Some of the tubes used in this research were faced on a lathe prior to welding. HSS bits were used, and most of the process was the same as for facing less-machinable alloys of stainless steel, except that the tools were fed in the opposite direction. The tools were fed into the workpiece with the relief angle first, and the cutting point last. This is illustrated in Figure 4.1. It is not known why this feed direction worked better, but it was found through trial and error.

4.5.7 Drilling Pin Holes

Pin holes were drilled in many NiTi tubes on a milling machine with straight-flute solid carbide drill bits, turning at about 100 rpm, while the tube was held rigidly in a vice. Started holes were made with HSS center drills, and although these center drills

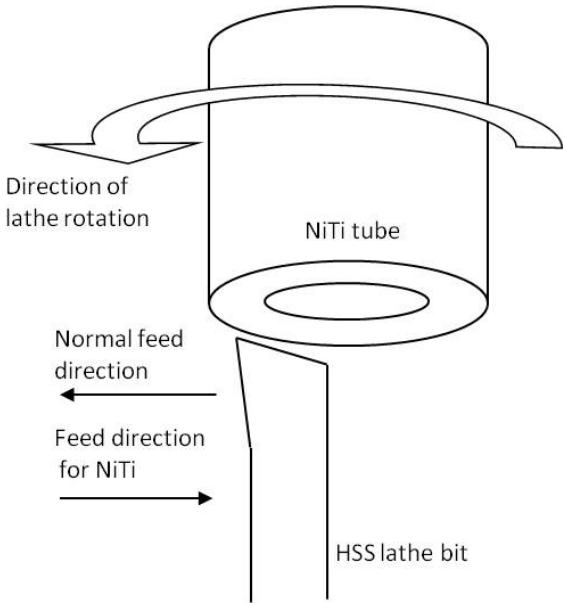

Figure 4.1: Diagram of facing a NiTi tube on a lathe.

can be used to drill all the way through the tube walls, it was found to be easier to finish the holes with the carbide drill bits. Fast rotational speeds and high pressure on the drill bits caused chattering and broke bits. Low rotational speeds and light pressure on the drill bits worked well. With these parameters described, one carbide drill bit could be used to make about five to ten holes before it became too dull to drill well. These 1/8" (3 mm) diameter bits were purchased for $10 to $15 each, so each hole cost about $2 to make.

4.6 Future Work

This last section describes work that will be performed in the future to build upon the findings presented in this thesis. Some future work can also be found in Section 3.3.6 which describes a statistical design of experiment to optimize the TIG

welding process, and Section 3.4.4 which describes high-temperature and cyclic testing on adhesively bonded specimens.

- Adhesive specimens will be sectioned to investigate the interface of the adhesive and the NiTi tubes and Al 2024 blocks. This sectioning will also check how uniform the adhesive gap is between the tubes and blocks.

- The high-temperature strength and fatigue properties of welded joints will be investigated. High-temperature ultimate failure tests and thermomechanical cycling tests will be run, similar to the tests run on adhesive specimens in Section 3.4.4. These properties are critical to know for the joints to be used in an actuator

- The compliance of the torsional testing machine (Figure 2.1) will be analyzed by monitoring its deformation during a test with a digital image correlation (DIC) system. The motor, gearbox, and main shaft supports are mounted on a 4" (102 mm) square, 0.125" (3 mm) wall thickness steel tube, and how much this tube and the rest of the machine deforms when a torque of 500 in-lb (57 N-m) is applied to a specimen will be measured.

- The alignment of the specimen grips will be more thoroughly investigated than it has been. Previously, the machine was aligned with a dial indicator. The strain field on the surface of a specimen will be measured with a DIC system to verify that the specimen is being loaded purely in shear. Any bending moments will be detected by the effect they have on the strain field.

Appendix A: ALL ADHESIVE STRENGTH DATA

Spec.	Grip	Adhesive	Overlap (in)	Mis-alignment (deg)	Judged Quality	Test	Temp. (°C)	Meas. Failure Torque (in-lb)	Quality Adjust-ment[b] (in-lb)	Al Grip Force	Al Grip Adjust-ment[c] (in-lb)	Adjusted Failure Torque (in-lb)
1	Solid	EA 9394	0.50	1.42	Bad	9	121	**189.8**	-15.3			**205.1**
2	Solid	EA 9394	0.50	1.27	Bad	10	20	**432.7**	-15.3			**448.0**
3	Solid	EA 9394	0.25	1.94	Bad	7	82	**122.6**	-15.3			**137.9**
4	Solid	EA 9394	0.25	1.73	Bad	6	20	**275.2**	-15.3			**290.5**
5	Solid	EA 9394	0.25	0.70	OK	8	121	**85.1**				**85.1**
6	Split	EA 9696	0.25	0.28	Bad	2	82	**209.0**	-15.3	Loose	5.34	**219.0**
7	Split	EA 9696	0.25	0.62	OK	1	20	**≥301.0**[a]		Tight	-5.34	**N/A**
8	Split	EA 9696	0.25	0.39	Bad	1	20	**318.5**	-15.3	Tight	-5.34	**339.1**
9	Split	EA 9696	0.50	0.71	OK	4	121	**93.5**		Loose	5.34	**88.2**
10	Solid	EA 9394	0.25	0.00	Good	6	20	**354.8**	13.4			**341.4**
11	Solid	EA 9394	0.25	0.13	Good	6	20	**355.3**	13.4			**341.9**
12	Solid	EA 9394	0.50	0.18	Good	9	121	**184.1**	13.4			**170.7**
13	Solid	EA 9394	0.50	0.04	Good	9	121	**221.7**	13.4			**208.3**
14	Solid	EA 9394	0.25	0.00	Good	7	82	**153.4**	13.4			**140.0**
15	Solid	EA 9394	0.25	0.12	Good	8	121	**113.5**	13.4			**100.1**
16	Solid	EA 9394	0.25	0.12	Good	8	121	**126.4**	13.4			**113.0**
17	Solid	EA 9394	0.25	0.00	OK	7	82	**160.5**				**160.5**
18	Solid	EA 9394	0.50	0.00	Good	10	20	**397.7**	13.4			**384.3**
19	Solid	EA 9394	0.50	0.24	Good	10	20	**≥373.1**[a]	13.4			**N/A**
20	Split	EA 9394	0.25	0.17	Good	5	20	**352.9**	13.4	Loose	5.34	**334.2**
21	Split	EA 9394	0.25	0.76	OK	5	20	**268.3**		Tight	-5.34	**273.6**
22	Split	EA 9394	0.25	0.12	Good	5	20	**324.4**	13.4	Tight	-5.34	**316.3**
23	Split	EA 9696	0.25	0.39	OK	3	121	**172.0**		Tight	-5.34	**177.3**
24	Split	EA 9696	0.25	0.01	OK	3	121	**178.0**		Tight	-5.34	**183.3**
25	Split	EA 9696	0.25	0.25	OK	2	82	**259.0**		Loose	5.34	**253.7**
26	Split	EA 9696	0.25	0.28	OK	3	121	**147.1**		Tight	-5.34	**152.4**
27	Split	EA 9696	0.25	0.68	OK	1	20	**361.2**		Loose	5.34	**355.9**
28	Split	EA 9696	0.25	0.27	OK	1	20	**363.9**		Loose	5.34	**358.6**
29	Split	EA 9696	0.25	0.13	OK	2	82	**288.7**		Tight	-5.34	**294.0**

[a] Specimens 7 and 19 broke at the pin holes, not in the adhesive bond.
[b] Quality adjustment from table 3.11.
[c] Clamping force adjustment from table 3.13.

Table A.1: All adhesive strength data and adjustments.

Bibliography

[1] S. Alapati, W. Brantley, J. Nusstein, G. Daehn, T. Svec, J. Powers, W. Johnston, and W. Gou. Vickers hardness investigation of work-hardening in used NiTi rotary instruments. *Journal of Endodontics*, 32:1191–1193, 2006.

[2] Darin Arbogast, Robert Ruggeri, and Richard Bussom. Development of a 1/4-scale NiTinol actuator for reconfigurable structures. volume **6930**. SPIE, 2008.

[3] Michael J. Cieslak. *ASM Handbook: Volume 6: Welding, Brazing, and Soldering*. ASM International, 1993.

[4] Simon Civjan, Eugene Huget, and Laszlo DeSimon. Potential applications of certain nickel-titanium (nitinol) alloys. *Journal of Dental Research*, 54(1):89–96, January 1975.

[5] Jack Collins. *Mechanical Design of Machine Elements and Machines*. John Wiley & Sons, 1st edition, 2003.

[6] Gordon Fox. Development of a characterization instrument for thermomechanical testing of shape memory alloy torque actuators. Undergraduate Honor's Thesis, The Ohio State University, Columbus, OH, 2010.

[7] Gordon Fox, Ryan Hahnlen, and Marcelo Dapino. Fusion Welding of Nickel Titanium and 304 Stainless Steel Tubes. Part 2. TIG Welding. Accepted in *Journal of Intelligent Material Systems and Structures*, January 2012.

[8] Ryan Hahnlen. Development and characterization of NiTi joining methods and metal matrix composite transducers with embedded NiTi by ultrasonic consolidation. Master's thesis, The Ohio State University, Columbus, OH, 2009.

[9] Ryan Hahnlen, Gordon Fox, and Marcelo Dapino. Fusion Welding of Nickel Titanium and 304 Stainless Steel Tubes. Part 1. Laser Welding. Accepted in *Journal of Intelligent Material Systems and Structures*, January 2012.

[10] Ryan Hahnlen, Gordon Fox, and Marcelo Dapino. Joining of Shape Memory NiTi to Aluminum 2024 Using Ultrasonic Soldering. *Welding Journal*, 2012.

[11] Peter Hall. US Patent 6875949: Method of welding titanium and titanium based alloys to ferrous metals, April 2005.

[12] Todd Hall. US Patent 5242759: Joint a Laminate and a Method of Preparing a Nickel-Titanium Alloy Member Surface for Bonding to Another Layer of Metal, September 1993.

[13] Darren Hartl and Dimitris Lagoudas. Characterization and 3-D Modeling of Ni60Ti SMA for Actuation of a Variable Geometry Jet Engine Chevron. SPIE, 2007.

[14] Dennis Kennedy, Friedrich Straub, L. Schetky, Saffir Chaudhry, and Richard Roznot. Development of an SMA Actuator for In-flight Rotor Blade Tracking. *Journal of Intelligent Material Systems and Structures*, 15, 2004.

[15] James Mabe, Dr. Robert Ruggeri, Ed Rosenzweig, and Chin-Jye Yu. NiTinol Performance Characterization and Rotary Actuator Design. volume **5388** of *Smart Structures and Materials 2004: Industrial and Commercial Applications of Smart Structures Technologies*. SPIE, 2004.

[16] Wolfgang Predki, Martin Klonne, and Adam Knopik. Cyclic torsional loading of pseudoelastic niti shape memory alloys: Damping and fatigue failure. *Materials Science & Engineering A*, 2005.

[17] Shankar Srinivasan. Lead-free Soldering for Auto Electronics Applications. Website: `http://www.ewi.org/aerospace`, 2010.

[18] Shelagh Thompson. An overview of nickel-titanium alloys used in dentistry. *International Endodontic Journal*, 33(4):297–310, July 2000.

[19] Casper van der Eijk, Hans Fostervoll, Zuhair K. Sallom, and Odd M. Akselsen. Plasma welding of NiTi to NiTi, stainless steel and Hastelloy c276. In *Conference proceedings ASM Materials Solutions*, 2003.

[20] Ge Wang. Welding of Nitinol to stainless steel. In *Proceedings of the International Conference on Shape Memory and Super Elastic Technologies*, pages 131–136, 1997.

[21] K. Weinert and V. Petzoldt. Machining of NiTi based shape memory alloys. *Materials Science and Engineering A*, 378:180–184, 2004.

[22] Ming H. Wu. Fabrication of Nitinol materials and components. In *Proceedings of the International Conference on Shape Memory and Superelastic Technologies*, pages 258–292, 2001.